

ARTICLE



Dysbindin-1A modulation of astrocytic dopamine and basal ganglia dependent behaviors relevant to schizophrenia

Rosa Mastrogiacomio^{1,11}, Gabriella Trigilio^{1,2,11}, Céline Devroye¹, Daniel Dautan^{1,3}, Valentina Ferretti¹, Gabriele Losi^{4,5}, Lucia Caffino⁶, Genny Orso⁷, Roberto Marotta¹, Federica Maltese¹, Enrica Vitali¹, Gessica Piras⁸, Alessia Forgiarini⁷, Giada Pacinelli¹, Annamaria Lia^{4,5}, Debora A. Rothmond⁹, John L. Waddington¹⁰, Filippo Drago², Fabio Fumagalli⁶, Maria Antonietta De Luca⁸, Gian Marco Leggio², Giorgio Carmignoto^{4,5}, Cynthia S. Weickert⁹, Francesca Managò^{1,12}✉ and Francesco Papaleo^{1,3,12}✉

© The Author(s), under exclusive licence to Springer Nature Limited 2022

The mechanisms underlying the dichotomic cortical/basal ganglia dopaminergic abnormalities in schizophrenia are unclear. Astrocytes are important non-neuronal modulators of brain circuits, but their role in dopaminergic system remains poorly explored. Microarray analyses, immunohistochemistry, and two-photon laser scanning microscopy revealed that Dys1 hypofunction increases the reactivity of astrocytes, which express only the Dys1A isoform. Notably, behavioral and electrochemical assessments in mice selectively lacking the Dys1A isoform unraveled a more prominent impact of Dys1A in behavioral and dopaminergic/D2 alterations related to basal ganglia, but not cortical functioning. Ex vivo electron microscopy and protein expression analyses indicated that selective Dys1A disruption might alter intracellular trafficking in astrocytes, but not in neurons. In agreement, Dys1A disruption only in astrocytes resulted in decreased motivation and sensorimotor gating deficits, increased astrocytic dopamine D2 receptors and decreased dopaminergic tone within basal ganglia. These processes might have clinical relevance because the caudate, but not the cortex, of patients with schizophrenia shows a reduction of the Dys1A isoform. Therefore, we started to show a hitherto unknown role for the Dys1A isoform in astrocytic-related modulation of basal ganglia behavioral and dopaminergic phenotypes, with relevance to schizophrenia.

Molecular Psychiatry (2022) 27:4201–4217; <https://doi.org/10.1038/s41380-022-01683-8>

INTRODUCTION

Dysbindin-1 (Dys1) protein, coded by the Dystrobrevin Binding Protein 1 (DTNBP1) gene, has been implicated in cognitive processes [1, 2], responses to antipsychotic drugs [1, 3, 4], and genetic risk for schizophrenia [3–5]. In agreement, dystrophin and its binding partners (Dys1 being a component of the dystrophin complex [6]) are implicated in schizophrenia by genome-wide studies [7], in line with previous linkage studies [8–11], and with evidence of reduced Dys1 levels in post-mortem brain samples from patients with schizophrenia [12, 13]. These clinical implications have been linked to Dys1-related modulation of neuronal dopaminergic and glutamatergic signaling [3, 4, 13–16], through receptor-mediated intracellular trafficking mechanisms, including D2-like receptors [1, 3, 6, 17].

Drosophila dysbindin (dDys) has shown dichotomic regulation of glutamatergic and dopaminergic transmission, with the latter involving glial cells [18]. Notably, an active role for astrocytes in dopaminergic signaling has emerged [19–22]. However, whether

Dys1 might participate in the machinery of astrocytic activity and related modulation of dopaminergic signaling is unexplored. Similarly, the behavioral implications of these astrocytic-related processes remain unknown. In mammals, Dys1 exists in at least three spliced transcripts, Dys1A, 1B, and 1C [6], with 1B not being revealed in mice, while 1A and 1C being orthologues in humans and mice [6, 15, 23]. These isoforms are believed to have distinct functions as they are differentially distributed in brain synaptosomes, are present in different functional domains, and have distinct binding partners [15, 24, 25]. However, the contribution of each Dys1 isoform in physiological functions, specifically in astrocyte-mediated processes, and the related behavioral outcomes, is unknown.

Here, we report that the Dys1A spliced transcript is implicated in astrocytic functioning, and related basal ganglia dopamine signaling and behavioral phenotypes. In particular, we show that clinically relevant Dys1 genetic hypofunction alter astrocyte activity. Furthermore, we find that Dys1A is the only isoform

¹Genetics of Cognition laboratory, Neuroscience area, Istituto Italiano di Tecnologia, via Morego, 30, 16163 Genova, Italy. ²Department of Biomedical and Biotechnological Sciences, University of Catania, Catania, Italy. ³Fondazione IRCCS Ca' Granda Ospedale Maggiore Policlinico, Milano, Italy. ⁴Neuroscience Institute, CNR, Padova, Italy. ⁵Department of Biomedical Science, University of Padova, Padova, Italy. ⁶Department of Pharmaceutical and Biomolecular Sciences, Università degli Studi di Milano, Milan, Italy. ⁷Department of Pharmaceutical and Pharmacological Sciences, University of Padova, Padova, Italy. ⁸Department of Biomedical Sciences, University of Cagliari, Cagliari, Italy. ⁹Schizophrenia Research Laboratory, Neuroscience Research Australia, Sydney, NSW, Australia. ¹⁰School of Pharmacy and Biomolecular Sciences, Royal College of Surgeons in Ireland, Dublin 2, Ireland. ¹¹These authors contributed equally: Rosa Mastrogiacomio, Gabriella Trigilio. ¹²These authors jointly supervised this work: Francesca Managò, Francesco Papaleo.

✉email: francesca.manago@iit.it; francesco.papaleo@iit.it

Received: 14 January 2022 Revised: 21 June 2022 Accepted: 27 June 2022

Published online: 11 July 2022

expressed in astrocytes and is preferentially involved in astrocytic, but not neuronal, Golgi morphology. Notably, selective disruption of *Dys1A* induces behavioral and dopaminergic alterations related to the basal ganglia, while sparing them at the cortical level. This might be clinically relevant as, in contrast to data from cortical samples, *Dys1A* is decreased in the caudate of patients with schizophrenia. We started to directly link these associations, demonstrating that disruption of *Dys1A* only in astrocytes recapitulate motivational, sensorimotor gating, dopamine and D2 expression alterations. Overall, we show a hitherto unknown implication of *Dys1A* in astrocytic and basal ganglia functioning, with relevance to schizophrenia.

MATERIALS AND METHODS

Mice

All procedures were approved by the Italian Ministry of Health (permit n. 230/2009-B, 107/2015-PR, and 749/2017-PR) and local Animal Use Committee and were conducted in accordance with the Guide for the Care and Use of Laboratory Animals of the National Institutes of Health and European Community Council Directives. Routine veterinary care and animal maintenance were provided by dedicated and trained personnel. Male and female littermate mice between 3 and 7 months of age were used. Animals were housed 2–4 per cage, in a climate-controlled animal facility ($22^{\circ}\text{C} \pm 2^{\circ}\text{C}$) and maintained on a 12 h light/dark cycle (08:00 on; 20:00 off), with food and water available ad libitum. The experimenter handled the mice on alternate days during the week preceding the tests. Body weight and general appearance of mice were recorded before and after behavioral testing.

***Dys1*, *Dys1A*, and *Dys1AGlast* mutant mice.** The *Dys1* heterozygous mutant mice (*Dys1* \pm) and their wild-type littermates (*Dys1* $+/+$), on C57BL6/J background were bred and used as previously described [1, 3]. The *Dys1A*_{flox/flox} mice generated by GlaxoSmithKline [26] were retained on C57BL6/J background and presented two loxP sites flanking exon 5, which is necessary for correct expression of the *Dys1A* long isoform. Constitutive *Dys1A* deletion (*Dys1A* $-/-$) or partial reduction (*Dys1A* \pm) was obtained crossing *Dys1A*_{flox/flox} mice with a germline Cre deleter transgenic strain (Taconic-Artemis Germany). The breeding scheme used consisted of mating one male *Dys1A* \pm with two *Dys1A* \pm females. Astrocyte-specific loss (*Dys1AGlast* $-/-$) or partial reduction (*Dys1AGlast* \pm) of the expression of *Dys1A* was obtained by mating *Dys1A*_{flox/flox} mice with the inducible Cre transgenic line *Glast-CreERT2* [27]. The resulting strain was then crossed with the reporter line stop_{flox/flox} tdTomato (Jackson Laboratory). Tamoxifen (T-5648, Sigma-Aldrich, St. Louis, MO, USA) was dissolved in corn oil (Sigma-Aldrich, C-8267) and 1:20 ethanol at 55°C for 2 h to prepare a stock solution at 100 mg/ml. Stock solutions were aliquoted and stored at -20°C . To induce Cre-mediated recombination, mice aged 60 days were administered tamoxifen 5 mg/day for 2 consecutive days by oral gavage [27]. Testing started 30 days later. The breeding scheme consisted of mating one *Dys1A*_{flox/+} *Glast-CreERT2*_{tg/tg} tdTomato_{flox/flox} male mouse with two *Dys1A*_{flox/+} *Glast-CreERT2*_{+/+} tdTomato_{flox/flox} female mice. Genotyping was performed by PCR using wild-type, targeted and Cre allele-specific primers. All mutant mice used were viable, fertile, normal in size and did not display any gross physical or behavioral abnormalities.

Microarray

Experiment were performed using Affymetrix GeneChip arrays as previously described [28]. **Processing and analyses.** We dissected the frontal cortex from: 11 females *Dys1* $+/+$, 13 males *Dys1* $+/+$, 15 females *Dys1* \pm , 10 males *Dys1* \pm , 12 females *Dys1* $-/-$, and 12 males *Dys1* $-/-$. Total RNA was extracted using TRIzol reagent (Life Technologies) and sent to the NIH National Human Genome Research Institute for hybridization to Affymetrix Mouse genome 430 2.0 arrays and scanning. Probe intensity values were extracted and probe sets were analyzed by Robust Multi-array Average (RMA).

Immunohistochemistry

Mice were deeply anesthetized (urethane 20%) and perfused transcardially with PBS followed by 4% formaldehyde solution (Sigma-Aldrich) in PBS, pH 7.4. Brains were extracted, post fixed overnight in 4% formaldehyde and cryoprotected in 30% sucrose in PBS. 40 μm -thick coronal sections containing region of interest were cut on a freezing microtome

(VT1000S, Leica Camera AG, Wetzlar, Germany) and collected in PBS before being processed for immunohistochemistry. For GFAP immunostaining, free-floating slices were first washed once in 0.3% Triton X-100 PBS (PBS-T) for 10 min, and twice with 0.1% PBS-T, then incubated for 1 h in a blocking solution of 5% normal goat serum in 0.1% PBS-T. Subsequently they were incubated overnight at 4°C with 1:300 rabbit polyclonal anti-GFAP antibody (Novus Biologicals, Centennial, CO, USA) in blocking solution. Between steps four washes in blocking solution were applied for 10 min. Slices were then mounted with ProLong™ Gold Antifade Mountant (ThermoFisher Scientific) and imaged in an inverted laser scanning confocal microscope (A1 Nikon, Shinjuku, Japan) using a 20 \times or 40 \times objective. Quantification and analysis were performed using Fiji software (Wayne Rasband, NIH, USA), outlining regions of interest. To analyze the number of *Glast*-positive cells in GPe sections, $\times 20$ magnification confocal images were acquired. For each animal three images were taken from sliced collected between 0.58 and -0.70 mm from Bregma. *Glast*-positive cells were quantified by averaging the cell density within and across each animal from 10 μm maximum projections images. Counts were performed using 3D objects counters tool provided by NIH ImageJ software and the subsequent analyses were performed following a blind procedure. Astrocyte surface and relative intensity were calculated analyzing GFAP signal in GFAP- and *Glast*-positive cells from 10 μm maximum projection images, acquired at $\times 40$ magnification.

Stereotaxic injections

All surgeries were performed under aseptic conditions. Mice were deeply anesthetized by inhalation of a mixture of isoflurane/oxygen (2%/1%) and mounted into a stereotaxic frame (David Kopf Instruments, Tujunga, CA, USA). Following shaving and preparation of the skin, a cranial hole was made above the targeted area. All measurements were made relative to bregma, in accordance with the mouse brain atlas [29]: GPe (AP: -0.4 , ML: 1.9 and DV: 3.7), PFC (AP: $+1.9$ mm; ML: ± 0.3 mm; DV: -2.4 mm).

Ex vivo calcium signaling in astrocytes

The viral injection (60% AAV5.GfaABC1DcytoGCaMP6f.SV40, 40% GfaABC1D-cyto-tdTomato.SV40, Addgene, Watertown, MA, USA) was performed using a borosilicate pipette at a rate of 50 nl/min using a 10 μl Hamilton syringe. After each injection, 10–15 min were allowed before slowly withdrawing the micropipette. Coronal slices of 300 μm were obtained from mice at postnatal days 90–120 three weeks after AAV injections. Animals were anaesthetized with isoflurane and the brain was removed and transferred into an ice-cold artificial cerebrospinal fluid (ACSF, in mM: 125 NaCl, 2.5 KCl, 2 CaCl_2 , 1 MgCl_2 , 25 glucose, pH 7.4 with 95% O_2 and 5% CO_2). Coronal slices were cut with a vibratome (VT1000S, Leica Camera AG) in the solution described in [30]. Then, slices were transferred for 1 min in a solution at room temperature (RT, in mM: 225 D-mannitol, 2.5 KCl, 1.25 NaH_2PO_4 , 26 NaHCO_3 , 25 glucose, 0.8 CaCl_2 , 8 MgCl_2 , 2 kynurenic acid with 95% O_2 and 5% CO_2). Finally, slices were transferred in sACSF at 32°C for 20 min and then maintained at RT for the entire experiment. To image Ca^{2+} dynamics in GCaMP6f-astrocytes, we used a two-photon (2P) laser scanning microscope (Multiphoton Imaging System, Scientifica Ltd., Uckfield, UK) equipped with a pulsed IR laser (Chameleon Ultra 2, Coherent, USA) tuned at 920 nm. Laser power at the sample was kept in the range 5–10 mW to avoid photostimulation and photobleaching. The excitation wavelength used was 920 nm for both GCaMP6f and tdTomato. Images were acquired at 1.53 Hz acquisition frame rate, for 2 min, through a water-immersion objective (Olympus, LUMPlan FI/IR 20 \times , 1.05 NA). The field of view ranged between 700 \times 700 μm and 120 \times 120 μm depending on the zoom factor. Ca^{2+} signal recordings were performed in cortical layers II/III in PFC brain slices. Brain slices were continuously perfused in a submerged chamber at a continuous rate of 3 ml/min with the following (in mM): 120 NaCl, 2.5 KCl, 1 NaH_2PO_4 , 26 NaHCO_3 , 1 MgCl_2 , 2 CaCl_2 , 10 glucose, pH 7.4 (with 5% $\text{CO}_2/95\%$ O_2) at room temperature. Tetrodotoxin (1 μM ; Hellobio, Bristol, UK) was also added to the perfusion solution to block neuronal activity in all recordings. Detection of astrocyte region of interests (ROIs) displaying Ca^{2+} elevations was performed with ImageJ in a semi-automated manner using the GECQuant plugin [31]. The software was used to identify ROIs corresponding first to the soma ($>30\mu\text{m}^2$; confirmed by visual inspection), then to the proximal processes ($>20\mu\text{m}^2$ and not corresponding to the soma) and finally to the microdomains (between 2 and $20\mu\text{m}^2$ corresponding to neither the soma nor the proximal processes). All pixels within each ROI were averaged to give a single time course of fluorescence values, F(t). Analysis of Ca^{2+} signals was performed with ImageJ (NIH) and a custom software developed in MATLAB 7.6.0 R2008 A (Mathworks, Natick, MA, USA) [32]. To compare relative changes in fluorescence between

different cells, we expressed the Ca^{2+} signal for each ROI as $\Delta F/F_0 = (F(t) - F_0)/F_0$. F_0 was defined as the 15th percentile of the whole fluorescent trace for each ROI and considered as a global baseline. For each ROI we then defined as baseline trace the points of the $\Delta F/F_0$ trace with absolute values smaller than twice the standard deviation of the overall signal. Significant Ca^{2+} events were then selected with a supervised algorithm as follows. Firstly, a new standard deviation was calculated on the baseline trace, and all local maxima with absolute values exceeding twice this new standard deviation were identified. Secondly, among these events, we considered significant only those associated with local Ca^{2+} dynamics with amplitude larger than fourfold the new standard deviation. The amplitude of each Ca^{2+} event was measured from the 20th percentile of the fluorescent trace interposed between its maximum and the previous significant one. Essentially, this procedure combines a threshold measured from the global baseline with a stricter threshold computed from a local baseline. We adopted this method to reduce artifacts from the recording noise superimposed on the slow astrocytic dynamics. All Ca^{2+} traces were visually inspected to exclude the ROIs dominated by noise. For each astrocyte we calculated the number of active ROIs, defined as the ROIs displaying at least one significant Ca^{2+} event, the frequency, i.e., the total number of Ca^{2+} events per minute and the mean amplitude of the Ca^{2+} events. For each parameter, we then calculated the mean value among all analyzed astrocytes.

Cell cultures

Astrocyte-enriched cell cultures were obtained from cortices dissected from postnatal day 1 (PND1) mice. Pups were sacrificed by cervical dislocation and cortices were quickly dissected in ice-cold HBSS (Hanks' Balanced Salt Solution, Gibco ThermoFisher Scientific). Samples were incubated in HBSS with 0.125% Trypsin-EDTA (ThermoFisher Scientific) and 1 mg/mL DNAase I (Sigma-Aldrich) for 20 min at 37 °C. A solution of DMEM (Dulbecco's Modified Eagle Medium, Gibco ThermoFisher Scientific) with 10% horse serum and 1% Penicillin-Streptomycin (Sigma-Aldrich) was added to the samples, which were then centrifuged at 1200 rpm and washed twice in complete medium. Samples were dissociated mechanically in complete medium and filtered through 40 μm cell strainers. Cell suspensions were finally plated on poly-D-lysine coated plates. Cells were cultured until 100% confluence. Neuronal cell cultures were obtained from E18 mice embryos. Cortices were dissected in ice-cold HBSS and incubated in HBSS with 0.125% Trypsin-EDTA and 0.25 mg/mL DNAase I for 30 min at 37 °C. A solution of Neurobasal™ medium (Gibco ThermoFisher Scientific) with 10% inactivated fetal bovine serum (Sigma-Aldrich), 1% penicillin-streptomycin, 1% GlutaMAX™ Supplement and 2% B27™ Supplement (Gibco ThermoFisher Scientific) was added to the samples, which were then centrifuged 1200 rpm and resuspended in complete medium before mechanical dissociation. Samples were filtered with 40 μm cell strainers, centrifuged 700 rpm and resuspended in complete medium. Cell suspensions were finally plated on poly-D-lysine coated plates. Neurons were cultured until complete maturation.

Western blot

For western blot analysis of Dys1 isoforms, we used Dys1^{+/+} mice at embryonic stage E14.5, PND7, PND35 and PND90, Dys1 and Dys1A knockout mice, glial and neuronal cell cultures. Animals were sacrificed by cervical dislocation; brains were rapidly dissected and stored at -80°. Tissues or cultured cells were lysed in RIPA buffer and Protease Inhibitor Cocktail (Sigma-Aldrich). Western blot analysis was performed using mouse polyclonal anti-dysbindin antibody (PA3111 validated and produced by [6], and anti-actin antibody (Sigma-Aldrich). Each antibody detects both Dys1 isoforms. Protein (25 μg) from precipitated homogenates was separated on SDS-PAGE, electro-transferred onto nitrocellulose membranes, and then probed with primary antibodies: mouse monoclonal anti-dysbindin antibody (1:1000) and mouse anti-actin antibody (1:10000). Immune complexes were detected using appropriate peroxidase-conjugated secondary antibodies (Thermo Fisher Scientific) and a chemiluminescent reagent (ECL prime; GE Healthcare Europe GmbH, Milan, Italy). Densitometric analysis was performed using ImageQuantTL software (GE Healthcare Europe GmbH). Results were normalized to respective control conditions. For western blot analyses in globus pallidus externus (GPe), GPe were homogenized in a glass-glass potter in cold 0.32 M sucrose buffer pH 7.4 containing 1 mM HEPES, 0.1 mM PMSF, in presence of commercial cocktails of protease (Roche, Monza, Italy) and phosphatase (Sigma-Aldrich, Milan, Italy) inhibitors and then sonicated. Total proteins have been measured in the total homogenate according to the Bradford Protein

Assay procedure (Bio-Rad, Milan, Italy), using bovine serum albumin as calibration standard. 10 μg of proteins for each sample were run on a sodium dodecyl sulfate-10% polyacrylamide gel under reducing conditions and then electrophoretically transferred onto nitrocellulose membranes (GE Healthcare, Milan, Italy). Blots were blocked 1 h at room temperature with I-Block solution (Life Technologies Italia, Italy) in TBS + 0.1% Tween-20 buffer and then incubated with antibodies against the total proteins of interest. The conditions of the primary antibodies were the following: anti-RAB5 (1:2000, Cell Signaling Technology Inc., RRID: AB_823625), anti-RAB9 (1:2000, AbCam, RRID: AB_303323), anti-GALT (1:1000, AbCam, Cat# ab178406), anti-GM130 (1:1000, Sigma-Aldrich, RRID: AB_532244), and anti- β -Actin (1:10000, Sigma-Aldrich, RRID: AB_476697). Expression levels of every single protein were normalized using its own β -Actin loading control, which was detected by evaluating the band density at 43 kDa. Optic density (OD) of immunocomplexes was visualized by chemiluminescence using the Chemidoc MP Imaging System (Bio-Rad Laboratories, RRID: SCR_008426). Gels were run two times each and the results represent the average from two different runs. We used a correction factor to average the different gels: correction factor gel 2 = average of (OD protein of interest/OD β -actin for each sample loaded in gel 1)/(OD protein of interest/OD β -actin for the same sample loaded in gel 2) [33].

Behavior

Locomotor activity. Mice were tested in an experimental apparatus consisting of four gray, opaque open field boxes (40 × 40 × 40 cm) evenly illuminated by overhead lighting (5 ± 1 lux). Each session was video-recorded using an overhead camera from ANY-maze (Stoelting Co., Wood Dale, IL, USA) with the experimenter absent from the room during the test. Activity was tracked during the first exposure to the empty open field arena for 30 min. For amphetamine experiments, mice were tested in the same open field arenas. First, mice were placed in the empty open field and allowed to explore for 10 min. Then, mice were removed from the arena, injected with 1.5 mg/kg/10 ml D-amphetamine sulfate (i.p.; Sigma-Aldrich) and returned to the open field for an additional 60 min. This procedure was repeated for 5 consecutive days. All sessions were videotaped and tracked with ANY-maze software (Stoelting Co.).

Male-female social interaction. The test was conducted in Tecniplast cages (35 × 23 × 19 cm) illuminated (5 ± 1 lux) and video-recorded using a Unibrain Fire-i digital camera. The video camera was mounted facing the front of the cage to record the session for subsequent scoring of social investigation parameters as previously described [34]. Unfamiliar female stimulus mice in estrus were matched to the subject male mice by age and maintained in social groups of four per home cage.

Social habituation/dishabituation task. Naive mice were tested in Tecniplast cages (35 × 23 × 19 cm) illuminated (5 ± 1 lux) and video-recorded using a Unibrain Fire-i digital camera. As described previously [34], mice were placed individually for environmental habituation to the test cage 1 h prior to testing. A stimulus mouse (unfamiliar of the same sex) was introduced into the testing cage for a 1 min interaction. At the end of the 1 min trial, the stimulus animal was removed and returned to an individual holding cage for 3 min. We repeated this sequence for three trials with 3 min inter-trial intervals. In a fifth 'dishabituation' trial, we introduced a new (unfamiliar) stimulus mouse into the testing cage. Videos of behaviors were recorded and subsequently scored offline.

Attentional set-shifting task. Attentional set-shifting was tested in the two-chamber intradimensional/extradimensional (ID/ED) Operon task as previously described [3, 35]. After random selection of mice for the ID/ED task, all behavioral parameters were obtained blind to the genotype of the animals. For habituation to the apparatus, during the first 2 days mice were habituated for 45 min to the apparatus with only neutral stimuli (Habituation 1) and trained to move from one chamber to the other (Habituation 2). Any nose poke into the nose-poke holes resulted in a pellet delivery into the food receptacle. The next day, mice were trained to perform two randomly presented simple discriminations (SDs) (e.g., between smooth vs sand cardboard; light on vs light off; peach vs sage) so that they were familiar with the stimulus dimensions (Habituation 3). These exemplars were not used again. The mice had to reach a criterion of eight correct choices out of ten consecutive trials to complete this and each following testing stage. Performance was measured in all phases of all experiments using number of trials to reach the criterion; time (in minutes) to reach the criterion and time (in seconds) from breaking the photobeams

adjacent to the automated door to a nose-poke response (latency to respond). A session started when a mouse was placed in one of the two chambers where all the stimuli were neutral. Then the transparent door was dropped to give the mouse access to the other chamber where the stimuli cues were on. The series of stages comprised a SD, compound discrimination (CD), compound discrimination reversal, intradimensional shift (IDS), IDS reversal (IDSRe), a second IDS (IDS2), IDS2 reversal (IDS2Re), extradimensional shift (EDS), and EDS reversal. The mice were exposed to the tasks in this order so that they could develop a set, or bias, toward discriminating between the correct and incorrect nose poke hole.

Acoustic startle response and prepulse inhibition (PPI). Acoustic startle response and PPI were measured using SR-Lab Systems (San Diego Instruments, San Diego, CA, USA) and TSE Startle Response System (TSE Systems GmbH, Bad Homburg, Germany) following previously described protocols [1, 36]. Briefly, a sudden acoustic stimulus (120 dB) elicits the startle response, while an acoustic, non-startling pre-pulse (74; 78; 82; 86; 90 dB) preceding the startle stimulus inhibits the startle response (PPI). The startle response elicited by sudden sensory stimuli and its PPI are among some of the most widely studied phenotypes that are highly conserved across mammalian species. A background level of 70 dB white noise was maintained throughout the test session.

Progressive ratio test. We tested mice in a motivational nose-poke operant paradigm for 14 mg 5-TUL pellets (Test Diet) as described previously [37]. To avoid confounding factors linked to food restriction/deprivation experience, mice were always provided with food and water ad libitum. The operant chambers used (MED Associates Inc, VT, USA) were equipped with two nose-poke holes mounted at the left and right of a central food magazine, each equipped with infrared photobeams connected to a computer with MED-PC V software. Nose poking into one of the two holes resulted in pellet delivery (active hole), whereas nose poking into the other hole (inactive hole) triggered the house light for 5 s (left and right randomly assigned and balanced between groups). Free water was available all times via a water bottle dispenser. Pellets were delivered to the food magazine by an automated dispenser situated outside the experimental chamber. Mice were placed into the operant chambers in the evening around 17:00 and taken out the following morning around 9:00–10:00. Lights within the sound attenuating boxes in which the operant chambers were located ensured mice experienced a light/dark cycle identical to that of holding rooms. Training and testing started automatically from the beginning to the end of the dark phase (20:00–8:00). Initially, a fixed ratio (FR)–1 reinforcement schedule was applied, i.e., one nose poke in the active hole resulted in delivery of one pellet. Mice were exposed to the FR1 schedule until they reached the criterion of >80% active pokes during the entire night for two consecutive nights. Mice that met this learning criterion were switched to a FR3 reinforcement schedule, i.e., three nose-pokes in the active hole produced delivery of one pellet. The FR3 reinforcement schedule lasted two nights if mice met the criterion of >80% active pokes during the entire night. Afterward, mice were exposed to a progressive ratio (PR) schedule that lasted 2 h from the beginning of the night phase and was changed nightly; first night: PR3; second night: PR6; and third night: PR9. Mice were returned to their home cage after the PR test. During the PR experiment, the number of active nose-pokes required to obtain each successive food pellet was progressively increased by three (PR3, 3n + 3), six (PR6, 6n + 6) and 9 (PR9, 9n + 9; where n = number of pellets earned). For example, in PR3 earning the first reinforcer required three active nose pokes, the second six nose pokes, the third nine nose pokes, etc. Likewise, in PR9 earning the first reinforcer required 9 active nose-pokes, the second eighteen nose-pokes, the third twenty-seven nose-pokes, etc. Following each PR session, we calculated the breakpoint (BP) as the last ratio level completed before the end of the 2 h testing session. For example, under the PR3 or the PR9 reinforcement schedules, to earn the third food pellet a mouse had to poke 3 + 6 + 9 or 9 + 18 + 27 times in the active hole, and thus was given a BP value of 9 or 27, respectively. The BP is a well-validated measure reflecting the strength of the reinforcer and the motivational state of the animal [37].

Slice surface biotinylation

These experiments were performed as previously described [1, 3]. Mice were anesthetized with isoflurane and decapitated. The brain was sectioned in cold carboxygenated HBSS enriched with 4 mM MgCl₂,

0.7 mM CaCl₂ and 10 mM D-glucose, and equilibrated with 95% O₂ and 5% CO₂ to yield pH 7.4, on a vibrating microtome at a thickness of 300 μm. Dorsal striatum (STR) and prefrontal cortex (PFC) were dissected from coronal slices. Before starting the surface biotinylation reaction, and to ensure a gradual cooling of the cells, the tissues were washed twice for 5 min in ice-cold HBSS buffer. The filters holding the tissues were transferred to a well containing an excess of biotinylation reagent solution of 100 μM NHS-LC-biotin (Pierce, Appleton, WI, USA) in HBSS. After 45 min of incubation, the tissues were transferred to another well and washed twice with HBSS buffer containing 200 mM Lysine (Sigma-Aldrich) to block all reactive NHS-LC-biotin in excess. The tissues were washed twice with ice-cold HBSS and immediately placed on ice to mechanically disrupt the tissue in 120 μl of lysis buffer (1% TX-100, PBS1X and a cocktail of protease inhibitors (Sigma-Aldrich)). To discard extra debris, homogenates were centrifuged for 5 min at 4 °C at 13,000 rpm and supernatants were collected. To precipitate the biotinylated proteins from the homogenates 50 μl of immobilized Streptavidin beads (Pierce) were added to the samples and the mixture was rotated for 3 h at 4 °C. The precipitates were collected by brief centrifugation, mixed with 50 μl of SDS-PAGE loading buffer, boiled for 5 min and stored at –80 °C until use. Protein extracts were separated on precast 10% SDS/PAGE (Bio-rad, Milan, Italy) and transferred to nitrocellulose membranes. Blots were incubated with primary antibodies overnight at 4 °C. Antibodies used were dopamine D2 receptor (sc-5303, Santa Cruz Biotechnology, Dallas, TX, USA, and AB5084P, Millipore), Synaptophysin (sc-365488, Santa Cruz Biotechnology) and Transferrin Receptor (sc-21011, Santa Cruz Biotechnology). Immune complexes were detected using appropriate peroxidase-conjugated secondary antibodies (Thermo Fisher Scientific) and a chemiluminescent reagent (ECL prime; GE Healthcare Europe GmbH, Milan, Italy). Densitometric analysis was performed by ImageQuantTL software (GE Healthcare Europe GmbH). Results were normalized to respective control conditions.

Chromatographic analyses of dopamine, DOPAC, HVA, NA, 5HT, and 5HIAA

Ex vivo tissue collection. Brains were harvested following rapid decapitation and sliced in 1 mm sections in a chilled stainless-steel mouse brain matrix. Slices were frozen on glass slides mounted on dry ice. Using a 2 mm biopsy punch, bilateral PFC, STR and GPe tissues were collected accordingly to the mouse brain atlas [29], and stored at –80 °C until neurochemical analyses.

In vivo microdialysis. Microdialysis procedure was performed as previously described [1, 3]. A concentric dialysis probe with a dialyzing portion of 1 mm was prepared and stereotaxically implanted in the right GPe (coordinates of the dialyzing portion tip, in mm, relative to bregma, according to the atlas [29]: anteroposterior (AP) = –0.4, lateral (L) = + 1.9, ventral (V) = –4.5) under isoflurane anesthesia. After surgery, mice were housed individually to recover for 24 h. On the day of microdialysis, probes were perfused at a constant flow rate (1 μl/min), with artificial cerebrospinal fluid (aCSF, in mM: 147 NaCl, 4 KCl, 2.2 CaCl₂) by means of a microperfusion pump. After 30 min stabilization, samples were collected every 20 min and stored in dry ice until the end of the experiment. Three groups of three dialysates (1 h per group) were consecutively collected: “baseline” (aCSF perfusion), “quinpirole” (perfusion of 25 nM quinpirole), and “wash-out” (aCSF perfusion). At the end of the microdialysis experiment, brains were collected and sliced to check probe implantation; only data obtained from mice with probes correctly implanted in GPe were included in the results.

Quantification of monoamines and metabolites by HPLC. PFC, STR, and GPe tissue samples were lysed by sonication in 0.1 M perchloric acid, and centrifuged (15,000 × g, 10 min, 4 °C). The supernatant was filtered by centrifugation (20,000 × g, 5 min, 4 °C) in ultra-free microcentrifuge tubes (Millipore, Burlington, Massachusetts, USA). Supernatants obtained from PFC, STR or GPe samples, and from dialysates obtained from GPe in vivo microdialysis were injected (11 μl) into a high-performance liquid chromatography apparatus (Alexys UHPLC/ECD Neurotransmitter Analyzer, Antec Scientific, Zoeterwoude, The Netherlands), equipped with an autosampler (AS 100 UHPLC, micro, 6-PV, Antec Scientific). The mobile phase [containing (in mM) 100 phosphoric acid, 100 citric acid, 0.1 EDTA.2H₂O, 3 octanesulfonic acid. NaCl plus 8% acetonitrile, adjusted to pH 3.0 with NaOH solution (50%)] was delivered at 0.050 ml/min flow rate with a LC 110 S pump (Antec Scientific) through an Acquity UPLC HSS T3 column

(1 × 100 mm, particle size 1.8 μm; Waters, Milford, Massachusetts, USA). Detection of dopamine, DOPAC and HVA was confirmed and carried out with two systems. An electrochemical detector (DECADE II, Antec Scientific) equipped with a SenCell 2 mm glassy carbon working electrode (Antec Scientific) set at +600 mV vs Ag/AgCl. Output signals were recorded with Clarity (Antec Scientific). The second HPLC was equipped with a reversed-phase column (C8 3.5 μm, Waters, USA) and a coulometric detector (ESA Coulochem III; Agilent Software). The electrodes of the analytical cell were set at +350 mV (oxidation) and -200 mV (reduction). The mobile phase contained 50 mM CH₃COONa, 0.07 mM Na₂EDTA, 0.5 mM n-octyl sulfate, and 12% (v/v) methanol, the pH of mobile phase was adjusted with CH₃COOH to 4.21. The sensitivity of the assay for DA/DOPAC/HVA was 5 fmol/sample. For tissue sample analysis, data were normalized by tissue weight. Dialysate contents were converted into percentages of the average baseline level calculated from the three fractions of the first hour of collection ("baseline" period), and are expressed as averaged percentages of "baseline", "quinpirole" and "wash-out" periods, obtained in each experimental group.

Electron microscopy

Mouse brains were perfused with 4% formaldehyde and 2% glutaraldehyde and embedded as described previously [38]. Bright field transmission electron microscopy images were acquired from thin (70 nm) sections using a Gatan Orius SC1000 series CCD camera (4008 × 2672 active pixels) (Gatan, Pleasanton, USA), fiber optically coupled to high-resolution phosphor scintillator under a JEOL JEM-1011 transmission electron microscope (TEM) (JEOL, Tokyo, Japan) with thermionic source (W filament) and maximum acceleration voltage 100 kV. Neurons and astrocytes were identified as routinely performed [39, 40], mainly by following ultrastructural characteristics: nuclear size and shape, chromatin organization and presence of nucleoli, cytoplasm electron density, abundance of cytoplasmic organelles and presence inside the cytoplasm of intermediate filaments. Once the cell type was identified, the Golgi complexes were acquired at greater magnification. All transverse sections of the Golgi Complex (GC) were taken at the same magnification (×6000) and analyzed using point-counting procedures, with surface densities of Golgi Complex (S_vGC) and Cytoplasm (S_vCYT) determined according to Leitz ASM system. Moreover, a qualitative score from 1 to 3 was assigned by two different persons blind to the experimental groups to all GC: the maximum score (3) was given when finding a group of cisternae organized in stacks containing tubular and vesicular structures, as defined for GC, and the lower score (1) was given when GC structure was destroyed. Double tilt high angular annular dark field (HAADF) scanning TEM tomography was performed using a Tecnai F20 transmission electron microscope (FEI Company, Eindhoven, The Netherlands), equipped with a field-emission gun operating at 200 kV and a Gatan Ultrascan US1000 (Gatan, Pleasanton, USA) CCD camera. For 3D electron tomography reconstruction of the Golgi apparatus in Dys1± mouse astrocytes a 300 nm-thick section was tilted through ±60° with the following tilt scheme: 1° at tilt higher than ±30° and 2° intervals at intermediate tilts. The images were acquired using a HAADF detector at a magnification of ×40,000. Computation of each double tilt tomogram was performed by combining two tilt series taken around two orthogonal axes with the IMOD software package. 3D reconstruction was performed using Amira™ Software (Thermo Fisher Scientific).

Drosophila

Stocks and crosses. The UAS-Ddysb-RNAi *Drosophila* line (v34355) used in this study was obtained from VDRC (Vienna Drosophila Stock Center). The Gal4 activator lines tubulin-Gal4 (5138), repo-Gal4 (7415), and elav-Gal4 (458), and the transgenic lines UAS-GalT-GFP (30902), were obtained from the Bloomington Stock Center, Indiana University. Experimental crosses were performed at 28 °C. **Immunocytochemistry.** *Drosophila* immunostaining was performed on wandering third instar larvae reared at 28 °C. Third-instar larvae were dissected in PBS and fixed in 4% paraformaldehyde in PBS for 15 min, washed in PBS 0.1% Triton X-100 (PBTX), and incubated with primary antibody overnight, and secondary antibody for 1 h. The primary antibody anti-Repo-8D12 (1:200, DSHB) and anti-ELAV (1:200, DSHB) were used. Secondary antibody Cy5-conjugated Goat anti-Mouse IgG (115-175-003) was from Jackson Immuno Research, and was used at 1:500. Third instar larvae were then mounted with Mowiol 488 and imaged using a Nikon EZ-C1 confocal microscope equipped with a Nikon Plan APO 60.0×/1.40 oil immersion objective. Z-stacks with a step size of 1 μm were taken using identical settings. Each stack consisted of 15–20 plane images

of 10 animals per genotype. The images obtained were processed and analyzed using *ImageJ*. **Electron microscopy.** The TEM projections images of *Drosophila* brains were acquired from ultra-thin sections under a FEI Tecnai-12 transmission electron microscope (FEI Netherlands) as in ref. [41]. ***Drosophila* RNA Extraction and RT-PCR.** The relative *Ddysb* expression levels were determined by quantitative real-time PCR as in ref. [42]. Each biological sample was loaded in triplicate and the data provided represent the mean values of the three independent biological replicates. The *Drosophila* primer pairs used are: *rp49* Fw: 5'-AGGCCCAAGATCGTGAAGAA-3', Rv: 5'-TCG ATACCTTGGGCTTGC-3'; *dDysb* Fw: 5'-TAGAGATCCGTTGTCGCAAG-3', Rv: 5'-GGCATATTGCTGTTGAGAT-3'. **Quantification of Golgi apparatus surface in *Drosophila* brains.** To quantify Golgi surface, maximum intensity projections of the Z-stack were produced with *ImageJ*. The Z-stacks of the green channel were extracted to grayscale and then thresholded. Three Region of interest per animal were selected (7000 μm²) and percentage of the area occupied by GalT-GFP signal was measured using the "analyze particle" tool of Fiji software. Ten animals were analyzed per genotype.

Human samples

The mRNA expression values are referred to DTNBP1 NM_183040 gene expression in the human postmortem dorsolateral prefrontal cortex of normal subjects across lifespan. The data are available in the open access on-line application "The Brain Cloud", which allows the query of genome-wide gene expression data and their genetic control, <http://www.libd.org/braincloud>. We selected the single isoform values on the base of Illumina probes used for the quantification. The Illumina probes used to identify the human dysbindin-1 isoforms were, for Dysbindin-1A hHA -chr6:15632467-15632536, and for Dysbindin-1C the hHC -chr6:15735609-15735678, both referred to Human Assembly March 2006 (NCBI 36/hg18).

Caudate samples from 18 healthy control samples and 22 schizophrenia cases were obtained from the NSW Tissue Resource Center. The tissue was processed at Neuroscience Research Australia as approved by the University of New South Wales Human Research Ethics Committee (HREC 12435; Sydney, Australia). The rostral caudate was dissected from anatomically matched fresh frozen coronal sections cut at 60 μm through the head of the caudate. Caudate extracted samples (run in duplicates) were denatured in loading buffer 2×, and boiled for 5 min at 95 °C, then the denatured samples were centrifuged at 10,000 g for 5 min. Each lane was loaded with 20 mg of total protein, as in previous studies (Talbot et al. 2011; Tang et al. 2009).

Statistics

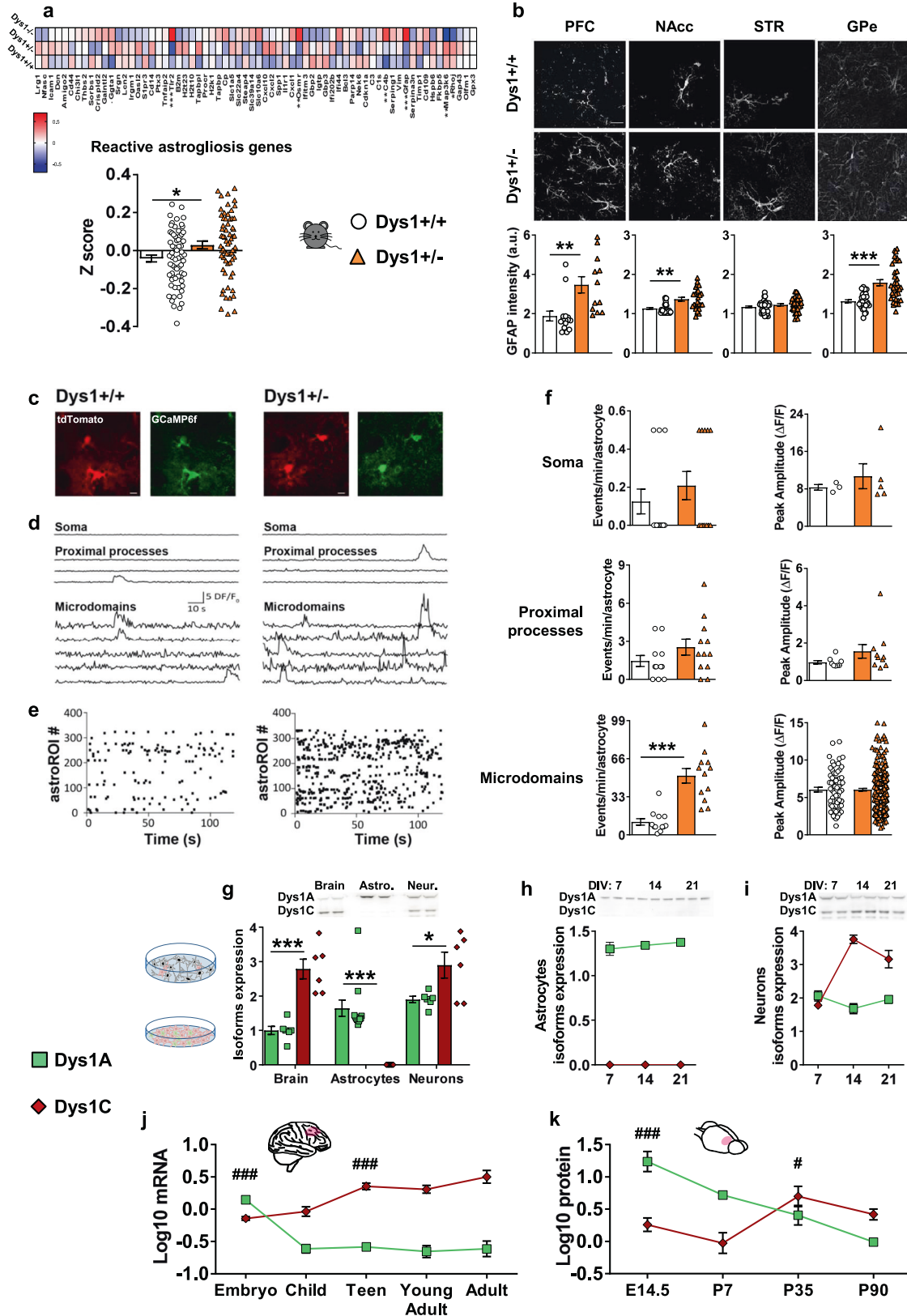
For animal experiments, no statistical methods were used to predetermine sample sizes, although sample sizes were consistent with those from previous studies [1, 3, 36, 43]. No explicit randomization method was used to allocate animals to experimental groups and mice were tested and data processed by investigators blind to animal identity. Statistical analyses were performed using commercial software (STATISTICA- 13.5, StaSoft, Tulsa, OK, USA, and Prism 7, GraphPad, San Diego, CA, USA). Results are expressed as mean ± standard error of the mean (SEM) throughout. Multiple Student's *t* tests, one-way and two-way ANOVAs were used, as appropriate, followed by Newman-Keuls' test for post hoc analysis and by Bonferroni correction. The accepted value for significance was *P* < 0.05. Data distribution was tested using the D'Agostino and Pearson normality test. The experiments reported in this work were repeated independently two to four times, using mice from at least four different generations. Numbers of mice are reported in the figure legends.

RESULTS

Dys1 hypofunction alters astrocytic reactivity

Unbiased microarray analysis showed in Dys1± and -/- mice, compared to Dys1+/+, increased expression of reactive astrogliosis-related genes (Fig. 1a and Supplementary Fig. S1), selected and analyzed based on [44]. To better investigate if more clinically-relevant Dys1 hypofunction (not complete ablation) might influence astrocytic activity, we then focused on Dys1 heterozygous mice (Dys1±), a model with direct translational validity for both healthy humans and patients with schizophrenia [1, 3].

Microarray indications were confirmed by higher immunoreactivity of the astroglial marker glial fibrillary acid protein



(GFAP) in Dys1[±] compared to Dys1^{+/+} littermates, which was similarly evident in PFC, and basal ganglia (NAcc and GPe) regions (Fig. 1b). By two-photon laser scanning microscope experiments in slice preparations from Dys1^{+/+} and Dys1[±]

mice we next evaluated Ca²⁺ signal dynamics in GCaMP6f-expressing astrocytes (Fig. 1c). We found that the number of spontaneous Ca²⁺ events occurring in astrocyte fine distal processes (i.e., microdomains) was markedly increased in Dys1[±]

Fig. 1 **Dys1 modulates astrocytic reactivity.** **a** Heat map of the relative expression of 65 reactive astrogliosis-related genes taken from a microarray screening from *Dys1*^{+/+} (n24), *Dys1*[±] (n25), and *Dys1*^{-/-} (n24) littermates. The heat map is based on hierarchical clustering of genes involved in astrogliosis as previously reported [44]. All gene expression levels were transformed to scores ranging from -0.5 to 0.5 and were colored blue, white, or red to represent low, moderate, or high expression levels, respectively. The relative expression levels were scaled based on their mean and do not represent expression levels in comparison with controls. *Dys1*[±] mice show higher expression for these genes compared to *Dys1*^{+/+} littermates (*t*-test: $t_{128} = -2.23$, $p = 0.028$). * $p < 0.05$ vs *Dys1*^{+/+}. **b** Quantification of cumulative GFAP intensity from confocal images from PFC, NAcc, STR and GPe displayed by *Dys1*^{+/+} and *Dys1*[±] littermates (n9 samples/brain region from each of n4 mice/genotype). Scale bars, 20 μ m (*t*-test, PFC: $t_{25} = -3.40$, $p = 0.0022$; NAcc: $t_{52} = -4.12$, $p = 0.00014$; STR: $t_{67} = -1.38$, $p = 0.17$; GPe: $t_{62} = -5.13$, $p < 0.0001$) ** $p < 0.005$, *** $p < 0.0005$ vs *Dys1*^{+/+}. **c** Representative confocal images of GFAP positive astrocytes in the analyzed brain regions. Two-photon images (average fluorescence of 2 min acquisition) of tdTomato (red) and GCaMP6f (green) expressing astrocytes in cortical slices from *Dys1*^{+/+} and *Dys1*[±] mice. Scale bars, 10 μ m. **d** Representative Ca^{2+} signal traces from the main astrocytic compartments. **e** Raster plots of Ca^{2+} transients from all GCaMP6 astrocyte microdomains in *Dys1*^{+/+} and *Dys1*[±] mice. **f** Mean number of events per minute per astrocyte and mean peak amplitudes of Ca^{2+} transients per active ROI in *Dys1*^{+/+} and *Dys1*[±] astrocytes (11 for *Dys1*^{+/+} and 12 for *Dys1*[±] mice, 4 animals each; microdomain events: *t*-test: $t_{22} = -5.83$, $p < 0.0001$). *** $p < 0.0001$ vs *Dys1*^{+/+}. **g** *Neuronal and astrocytic expression and developmental patterns of Dys1 isoforms.* **g** Representative western blots and densitometric analysis of *Dys1A* (50 kDa) and *Dys1C* (38 kDa) isoforms. β -actin used as loading control. In brain lysate of adult PND90 mice both isoforms were revealed, with higher expression for *Dys1C* compared to *Dys1A* (*t*-test: $t_{10} = -5.77$, $p = 0.0002$). *Dys1A* was the only isoform expressed in glial cells (*t*-test: $t_{20} = -6.32$, $p < 0.0001$). Similar to brain lysate, neuronal cultures show the expression of both isoforms with relative higher levels of *Dys1C* (*t*-test: $t_{10} = -2.57$, $p = 0.02$). **h** Astrocytes cultures at different developmental time points (day 7 = DIV7; day 14 = DIV14; day 21 = DIV21) confirming no expression of *Dys1C* in astrocytes. **i** Neuronal cultures at different developmental time points (DIV7, 14 and 21) showing relative higher expression of *Dys1C* compared to *Dys1A*. **j** mRNA expression of *Dys1A* and *Dys1C* isoforms from the human dorsolateral PFC by the open-access Brain Cloud databank at different developmental ages. Ns: Embryos = 38; Child = 32; Teen = 50; Young adult = 25; Adult = 122. *Dys1A* expression was highest at the embryonic stage and then decreased, while *Dys1C* expression increased from adolescence (two-way ANOVA, isoforms*age interaction: $F_{5,250} = 68.84$; $p < 0.0001$). *** $p < 0.0001$ vs consecutive ages for *Dys1A*, and vs preceding ages for *Dys1C*. **k** Protein expression of *Dys1A* and *Dys1C* isoforms from the mouse prefrontal cortex at different developmental ages. n6 mice/time point. *Dys1A* expression was highest at the embryonic stage and then decreased, while *Dys1C* expression increased from adolescence (two-way ANOVA, isoforms*age interaction: $F_{3,17} = 32.77$; $p < 0.0001$). * $p < 0.01$ and *** $p < 0.0001$ vs consecutive ages for *Dys1A*, and vs preceding ages for *Dys1C*. Bar graphs show mean \pm s.e.m.

mice compared to *Dys1*^{+/+} mice, while the mean Ca^{2+} peak amplitudes was unchanged (Fig. 1d, e, f). Ca^{2+} activity at soma and proximal processes showed no significant differences (Fig. 1d, e, f). These results confirm a hyperactivity of astrocytes in *Dys1* hypofunctioning mice.

Overall, these data provide initial evidence that reduced levels of *Dys1* influence astrocyte activity.

Distinct neuronal/astrocytic expression and developmental patterns of *Dys1* isoforms

We then asked whether *Dys1* isoforms might be differentially expressed in neurons and astrocytes.

Dys1A was expressed in adult mouse brain, in cultured astrocytes cells, and in cultured neuronal cells (Fig. 1g). In contrast, *Dys1C* was missing in astrocytes cells, while its expression was higher than *Dys1A* in the brain as well as in cultured neuronal cells (Fig. 1g). *Dys1A* showed a stable expression over time in glial and neuronal cultures, while *Dys1C* was always absent in astrocytes cultures and increased its expression over time in neuronal cells (Fig. 1h, i). We confirmed divergent developmental patterns of expression of these two *Dys1* isoforms, with similar findings in human and mouse brains. Specifically, samples of human dorsolateral PFC revealed higher *Dys1A* expression in the embryonic phase, which gradually decreased across development (Fig. 1j). Conversely, *Dys1C* expression was lower in embryonic and childhood stages and then increased from adolescence (Fig. 1j). Similarly, in mouse PFC the expression of *Dys1A* protein decreased from the embryonic phase, while *Dys1C* increased its expression in adolescence (Fig. 1k).

Overall, these data show a similar developmental pattern of *Dys1* isoforms expression between mice and humans, and define a previously unexpected constraint of *Dys1A* expression in astrocytes.

Dys1A disruption alters basal ganglia- but not cortical-dependent behaviors

The observation that only the *Dys1A* isoform is expressed in astrocytes prompted us to explore the effects of a selective *Dys1A* disruption using a mouse line with flanking *LoxP* sites targeted to

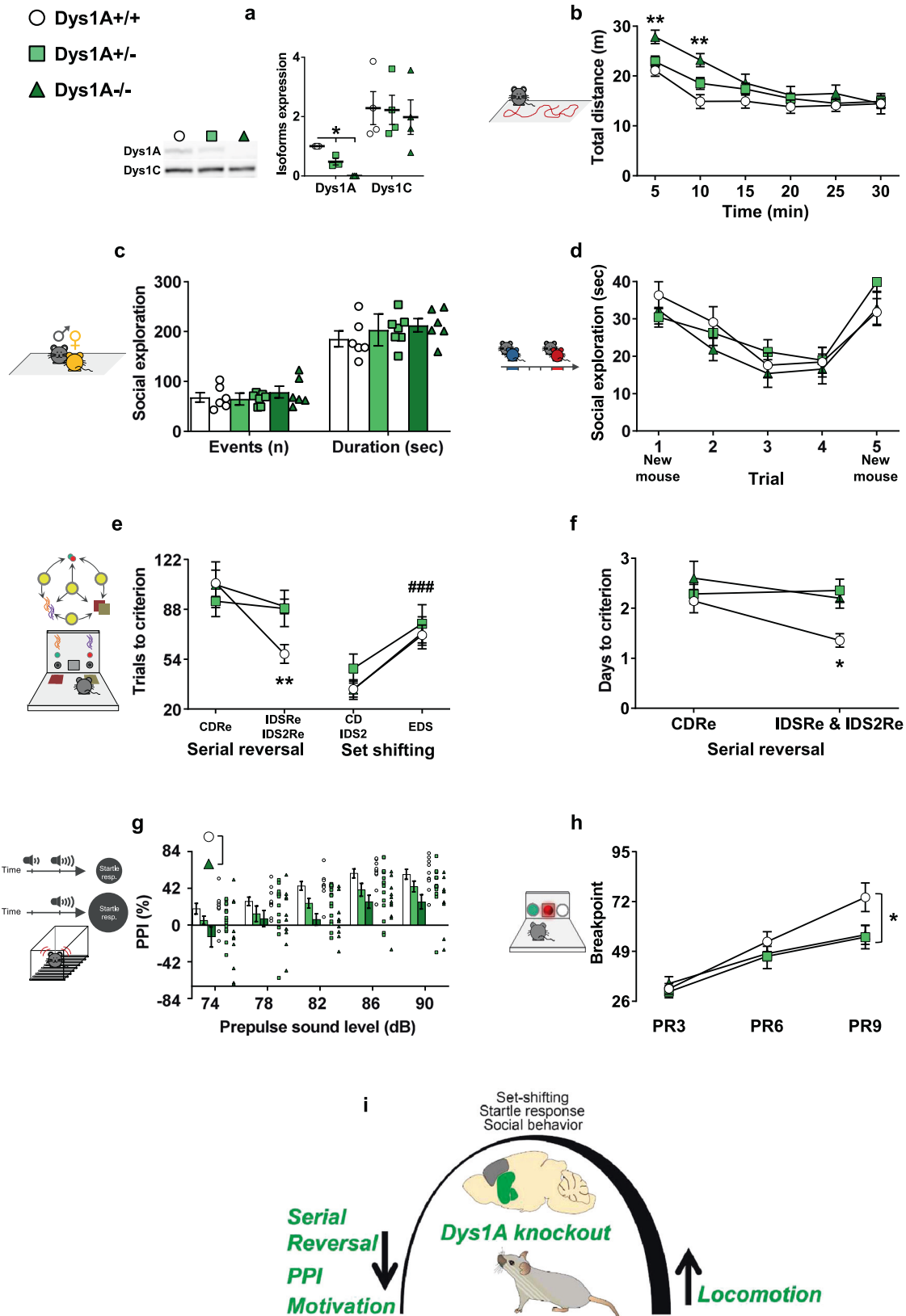
the exon 5 of *Dtnbp1* on chromosome 13a (*Dys1A*^{fl^{ox}/fl^{ox}}), backcrossed with a germline *Cre* deleter mouse line [26].

Dys1A[±] and *Dys1A*^{-/-} mice have a gene dosage-dependent reduction and lack of *Dys1A* isoform, respectively, and unaltered *Dys1C* expression (Fig. 2a and Supplementary Fig. S2). We then performed in *Dys1A* knockout mice a comprehensive battery of behavioral tests that were previously applied to mice with disruption of both *Dys1* isoforms [1, 3, 45, 46].

In agreement with an initial characterization [26], *Dys1A*[±] and *-/-* mice were viable with no evident alterations in general health and sensory functions. Similar to this previous study, *Dys1A*^{-/-} mice presented a hyperactive phenotype compared with *Dys1A*^{+/+} littermates (Fig. 2b), as in *Dys1* knockout mice [1, 46]. Moreover, as in *Dys1* knockout mice [46], locomotor responses to both acute and sub-chronic amphetamine were not affected by deletion of *Dys1A* (Supplementary Fig. S2). In *Dys1A*, in contrast to *Dys1* knockout mice [45, 47, 48], no alterations were evident in social interaction and social habituation/dishabituation (Fig. 2c, d). These results indicate that *Dys1A* is involved in locomotor activity, but not in social interactions.

Dys1 hypofunction is associated with PFC-dependent executive functions deficits in mice, healthy humans, and patients with schizophrenia [1, 3]. Thus, we tested *Dys1A* mice in the attentional set-shifting task (ASST), which allows assessment of discrete cognitive executive functions with translational validity to humans [3, 35]. In contrast to *Dys1* knockout mice [1, 3], *Dys1A*[±] and *-/-* mice show no deficits in extradimensional set-shifting (EDS) but serial reversal learning was altered (Fig. 2e, f). EDS alterations imply dopaminergic dysfunction in PFC [35, 49], while serial reversal learning is linked to dopaminergic tone in striatal regions [35, 50]. This prompted us to assess behaviors more related to basal ganglia dopamine-related functioning.

Prepulse inhibition (PPI) deficits are consistently linked to overactive dopamine/D2 signaling in basal ganglia [51–53]. We found a gene-dosage effect for reduced PPI in *Dys1A*[±] and *-/-* compared with *Dys1A*^{+/+} littermates (Fig. 2g). No *Dys1A*-dependent effects were evident for acoustic startle responses or body weight (Supplementary Fig. S2), excluding potential confounding factors.



Motivation to receive a reward is another behavioral trait strongly related to dopaminergic functioning within the basal ganglia [54–56]. We found reduced reward-motivated behavior in Dys1A± and -/- compared with Dys1A+/+ littermates (Fig. 2h),

when tested in a PR paradigm designed to assess motivational processes [37]. No Dys1A-dependent differences were present during acquisition phases (Supplementary Fig. S2), excluding deficits in motor coordination, learning and memory.

Fig. 2 **Dys1A disruption impairs basal ganglia- but not PFC-dependent behaviors.** **a** Selective reduction of Dys1A does not affect Dys1C expression. Western blots and densitometric analysis in Dys1A+/+, ± and -/- littermates. Expression of Dys1A (50 kDa), Dys1C (38 kDa). β -actin used as loading control. Expression of Dys1A is reduced in Dys1A± and absent in Dys1A-/- in PFC (one-way ANOVA, $F_{2,6} = 60.48$; $p < 0.0005$). * $p < 0.01$ vs Dys1A+/+ littermates. Expression of Dys1C was intact across all genotypes (one-way ANOVA, $F_{2,9} = 0.09$; $p = 0.92$). n4 mice/group. **b** Spontaneous distance traveled by Dys1A+/+ (n17), Dys1A± (n22) and Dys1A-/- (n10) during 30 min exposure to an open field arena. Dys1A-/- show increased locomotion during the first 10 min in the open field (Two-way repeated measure ANOVA, time*genotype interaction: $F_{10,215} = 3.04$; $p = 0.001$). ** $p < 0.005$ vs Dys1A+/+ at the same time point. **c** Male-female social interaction, displayed by Dys1A+/+ (n6), Dys1A± (n7) and Dys1A-/- (n6) littermates. No genotype-dependent difference was evident in the number of events or exploration time (two-way ANOVA; events: $F_{2,15} = 0.52$; $p = 0.60$; duration: $F_{2,15} = 0.75$; $p = 0.49$). **d** Social habituation-dishabituation, displayed by Dys1A+/+ (n14), Dys1A± (n16) and Dys1A-/- (n10) littermates. No genotype-dependent difference was evident (two-way repeated measure ANOVA genotype: $F_{2,37} = 0.37$; $p = 0.69$; genotype*time interaction: $F_{8,148} = 1.88$; $p = 0.07$). **e** Attentional Set-Shifting Test (ASST), performed in Dys1A+/+ (n14), Dys1A± (n14) and Dys1A-/- (n10) littermates. In contrast to Dys1A+/+, both Dys1A± and Dys1A-/- mice did not show the expected reduced trials to criterion in serial reversal stages (two-way repeated measure ANOVA; reversal stage: $F_{1,35} = 11.46$; $p = 0.002$; genotype*reversal stage interaction: $F_{2,35} = 4.27$; $p = 0.02$). ** $p < 0.005$ vs Dys1A± and -/- at the same time point. All mice showed the expected increase in trials to criterion at EDS stage independent of genotype (two-way repeated measures ANOVA; shifting stage: $F_{1,35} = 17.45$; $p = 0.0002$; genotype*shifting stage interaction: $F_{2,35} = 0.09$; $p = 0.92$). ### $p < 0.0005$ vs CD & IDS2 stages. Data for IDSRe & IDS2Re, CD & IDS2, IDSRe & IDS2Re refers to the average between the indicated stages as they are part of the same cognitive construct. **f** Days needed to reach criterion in ASST stages shown by Dys1A+/+ (n14), Dys1A± (n14) and Dys1A-/- (n10) littermates. In contrast to Dys1A+/+ mice, both Dys1A± and Dys1A-/- mice did not show the expected reduced days to criterion in serial reversal stages (two-way repeated measure ANOVA; reversal stage: $F_{1,35} = 5.01$; $p = 0.03$; genotype*reversal stage interaction: $F_{2,35} = 2.60$; $p = 0.05$). **g** Percent PPI of the 120 dB acoustic startle response displayed by Dys1A+/+ (n10), Dys1A± (n15) and Dys1A-/- (n12) littermates. Dys1A-/- have lower PPI compared to Dys1A+/+ mice (two-way repeated measure ANOVA; genotype: $F_{2,34} = 4.44$ $p = 0.019$). * $p < 0.01$ vs Dys1A+/+. **h** Breakpoint during a food-driven operant behavior test with increasing progressive ratio (PR) displayed by Dys1A+/+ (n12), Dys1A± (n13) and Dys1A-/- (n10) littermates. Both Dys1A± and Dys1A-/- mice showed lower breakpoints than Dys1A+/+ mice (two-way repeated measures ANOVA; genotype: $F_{4,64} = 2.8$; $p = 0.032$). * $p < 0.05$ vs Dys1A+/+. Bar and line graphs show mean \pm s.e.m. **i** Schematic drawing summarizing the behavioral data obtained in Dys1A knockout mice, pointing to a major alteration of basal ganglia-dependent, but not PFC-dependent, phenotypes.

Overall, these findings point to a more prominent involvement of Dys1A in behavioral phenotypes mediated by dopaminergic signaling in the basal ganglia (Fig. 2i).

Dys1A disruption alters dopamine/D2 homeostasis in basal ganglia, but not in PFC

Dopaminergic signaling in basal ganglia is implicated in locomotion, motivation, serial reversal learning, and PPI [50, 51, 53], which are altered in Dys1A knockout mice. Thus, we assessed Dys1A modulation of dopaminergic system in basal ganglia and, as comparison, in PFC.

We first revealed a higher expression of Dys1A protein in GPe compared to PFC and STR (Fig. 3a). Notably, GPe is an astrocyte-enriched brain region [20]. In contrast, Dys1C was equally expressed in all regions considered (Fig. 3b).

Dys1A disruption increased the expression of total D2 receptors in GPe, but not in PFC or STR (Fig. 3c). Moreover, Dys1A disruption increased cellular surface D2 receptors in STR and GPe, but not in PFC (Fig. 3d). Notably, disruption of both Dys1 isoforms resulted in comparable D2 alterations, but both in PFC and striatal regions ([1, 3] and Supplementary Fig. S3). Similarly, a Dys1A genotypic effect on dopamine content was present in GPe, but not in PFC and STR (Fig. 3e-g). In particular, Dys1A-/- mice had lower dopamine levels than Dys1A+/+ in GPe, and lower HVA levels in STR (Fig. 3f-g). DOPAC/dopamine and HVA/dopamine ratios were indistinguishable across genotypes in all regions, suggesting a normal rate of dopamine catabolism (Supplementary Fig. S3). No Dys1A genotype effects on levels of noradrenaline, serotonin, and 5HIAA were evident (Supplementary Fig. S3).

Consistent with our behavioral assessments, our data show that the selective disruption of the Dys1A isoform alters the dopaminergic system in basal ganglia, but not in PFC.

Dys1A hypofunction alters Golgi trafficking in astrocytes, but not in neurons

Dys1 influences the dopaminergic system by altering intracellular vesicular trafficking [17, 57, 58]. Thus, we first checked different markers of vesicular trafficking in GPe of Dys1A knockout mice. Our focus on GPe was driven by Dys1A-dependent dopaminergic alterations prevalently in this region (Fig. 3), and because this is an astrocyte-enriches area [20].

Dys1A disruption decreased the expression of Rab5 (Fig. 4a, Supplementary Fig. S4), that regulates the internalization and trafficking of membrane receptors (vesicle fusion and receptor sorting in the early endosomes), and Rab9 (Fig. 4b, Supplementary Fig. S4), a protein that mediates endosome-to-trans-Golgi Network (TGN) transport [59, 60]. Similarly, the trans-Golgi marker Galt [61] as well as the cis-Golgi marker GM130 [62] were both reduced in Dys1A knockout mice (Fig. 4c, d, Supplementary Fig. S4). These data indicate that disruption of the single Dys1A isoform generate alterations within the basal ganglia in proteins known to affect intracellular vesicular trafficking.

Using electron microscopy analyses, we then investigated if there could be any visible Dys1A-dependent morphological alteration in intracellular vesicles that differ between neuronal and astrocytic cells. Compared to Dys1A+/+, we found in Dys1A-/- mice more irregularly shaped and swollen cisternae of the Golgi complex with enlarged vesicle-like structures in astrocytic, but not neuronal cells (Fig. 4e and Supplementary Video V1). In contrast, deletion of all Dys1 isoforms disrupted Golgi complex morphology in an equivalent way, but in both neuronal and astrocytic cells (Fig. 4f). Equivalent results in altered Golgi complex morphology were obtained (Fig. 4g) by knocking down drosophila dDys either ubiquitously or in glial cells (Supplementary Fig. S5). Moreover, in drosophila, which don't have Dys1C, dDys downregulation did not alter Golgi morphology in neurons (Supplementary Fig. S5).

Overall, these findings support a more prominent role for Dys1A in basal ganglia astrocytic functioning.

Dys1A is reduced in the caudate of schizophrenia cases

To verify if Dys1A-modulation of basal ganglia-related phenotypes might have clinical relevance, we measured Dys1 isoforms in the caudate of schizophrenia cases and matched healthy controls (Supplementary Fig. S6). This revealed reduced Dys1A, but not Dys1C, in patients with schizophrenia compared with controls (Fig. 4h). Notably, previous findings reported reduced Dys1C, but not Dys1A, in the PFC of patients with schizophrenia [6]. To directly compare our results to these previous reports, we calculated a mean case-control ratio where zero indicates no differences between cases and controls, negative values reduced expression in schizophrenia, and positive values increased expression. In the caudate, Dys1A was reduced in 15 out of 22

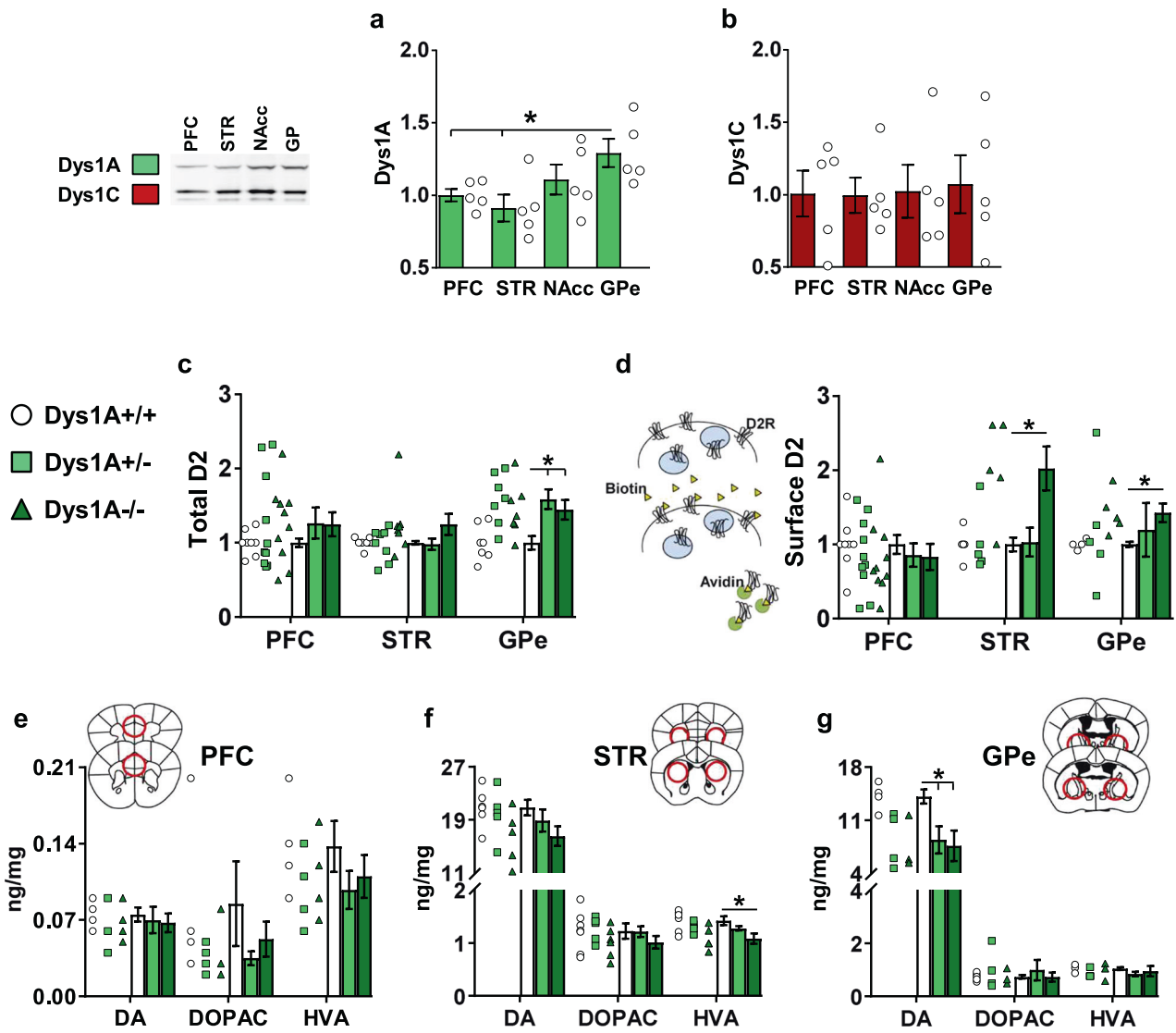


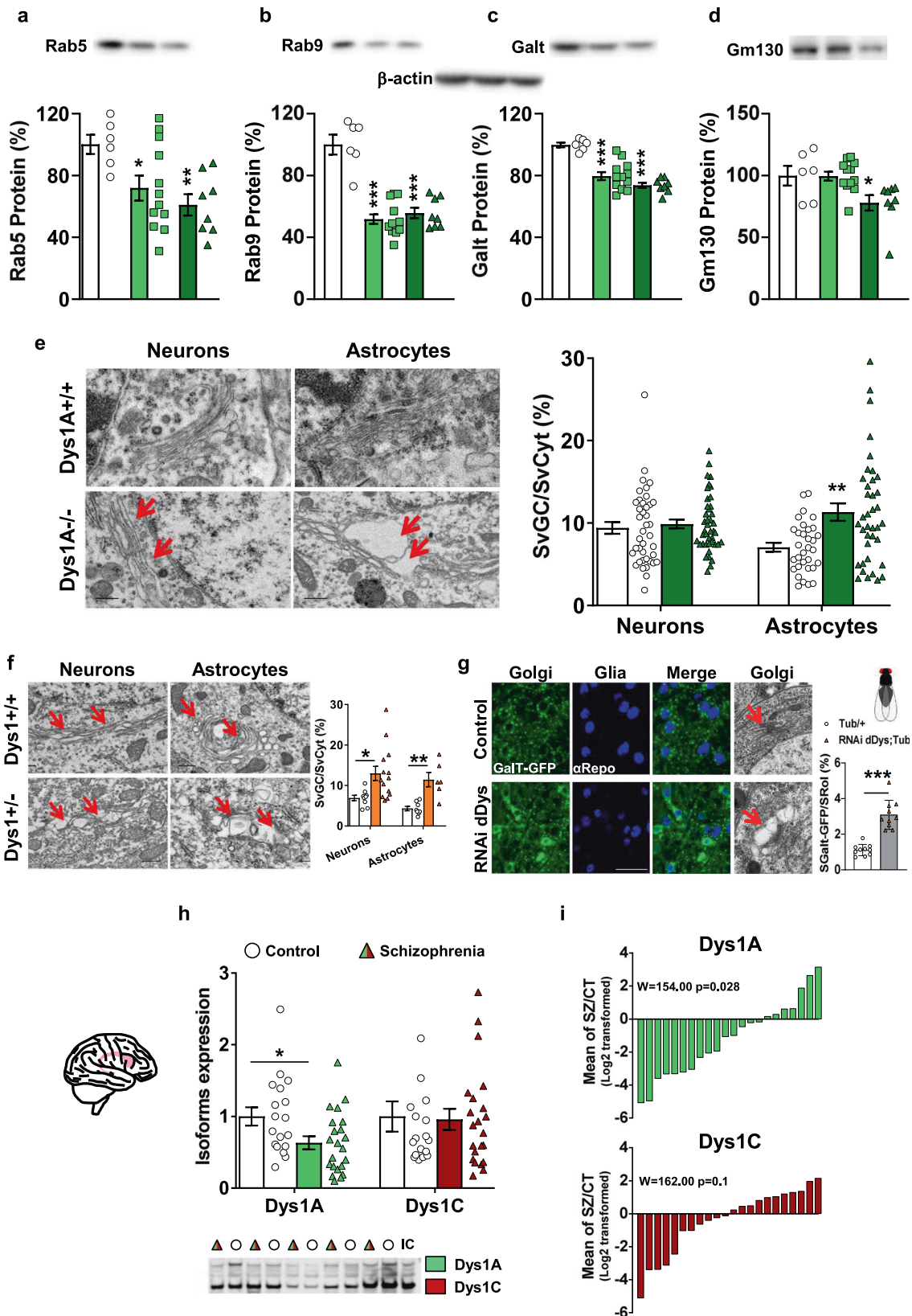
Fig. 3 **Dys1A alters the dopaminergic system within basal ganglia but not PFC.** Protein expression displayed by C57BL/6J adult mice of (a) Dys1A and (b) Dys1C isoforms in the PFC, STR, NAcc, and GPe relative to PFC and normalized to their own β -actin. Dys1A expression is higher in GPe compared to PFC and STR (one-way ANOVA: $F_{3,16} = 5.02$; $p = 0.02$). * $p < 0.05$ vs PFC and STR. Dys1C expression is uniform across the selected brain areas (one-way ANOVA: $F_{3,16} = 0.045$; $p = 0.98$). **c–d** D2 receptor expression in Dys1A^{+/+} (n9), Dys1A[±] (n10) and Dys1A^{-/-} (n10). Synaptophysin was used as cytoplasmic control, and D2 expression normalized on transferrin as loading control. **c** Dys1A[±] and Dys1A^{-/-} mice show increased total D2 expression compared to Dys1A^{+/+} in GPe (one-way ANOVA: $F_{2,16} = 4.93$; $p = 0.021$), but not in PFC ($F_{2,25} = 0.724$; $p = 0.49$), and STR (one-way ANOVA: $F_{2,22} = 1.44$; $p = 0.26$). **d** Biotinylation protocol for brain slices treated with biotin to label all surface proteins, precipitated by streptavidin. Dys1A^{-/-} mice have increased expression of D2 receptors on cellular surface compared to Dys1A^{+/+} littermates in STR and GPe (one-way ANOVA: STR $F_{2,14} = 4.20$; $p = 0.04$; GPe $F_{1,6} = 6.18$; $p = 0.04$), but not in PFC (one-way ANOVA: $F_{2,24} = 0.44$; $p = 0.64$). * $p < 0.05$ vs Dys1A^{+/+}. **e–g** Dopamine (DA), DOPAC, and HVA content by HPLC, expressed as ng/mg of tissue in (e) PFC, (f) STR, and (g) GPe dissected from Dys1A^{+/+} (n4), Dys1A[±] (n4), and Dys1A^{-/-} (n4) littermates. No Dys1A-dependent changes were observed in PFC (one-way ANOVA: $F_{2,5} = 0.23$; $p = 0.80$). Dys1A^{-/-} show reduced HVA levels relative to Dys1A^{+/+} in the STR (one-way ANOVA: $F_{2,14} = 4.72$; $p = 0.03$; Bonferroni correction $p < 0.05$). Dys1A[±] and Dys1A^{-/-} show reduced DA levels relative to Dys1A^{+/+} in GPe ($F_{2,10} = 6.91$; $p = 0.02$; Bonferroni correction $p < 0.05$). * $p < 0.05$ vs Dys1A^{+/+}. Bar graphs show mean \pm s.e.m.

case-control pairs, while Dys1C ratios were inconsistent in direction, and of generally smaller magnitude (Fig. 4i). No significant differences were found in the demographic variables of age, sex, pH, or PMI between the diagnostic groups (Supplementary Fig. S6). Together, these data suggest that, in contrast to PFC, Dys1A may have a role in basal ganglia-related schizophrenia pathobiology.

Selective disruption of Dys1A in astrocytes

Finally, to directly assess the role of astrocytic Dys1A in basal ganglia behavioral phenotypes, we backcrossed Dys1A^{flx/flx} with

inducible Glaxt CreERT2 mice (Fig. 5a). Selective deletion of Dys1A and expression of tdTomato reporter in astrocytes was triggered by tamoxifen injection in adult Dys1AGlaxt mice, to exclude developmental effects. Employing fluorescence-activated cell sorting (FACS), we isolated tdTomato-positive astrocytes from the striatal region (STR + GPe) of Dys1AGlaxt mice (Fig. 5b). We confirmed that these cells were enriched in Glaxt compared to tdTomato-negative cells (Fig. 5c). In agreement with previous reports [63], the GlaxtCreERT2 system was selective for astrocytes, as we found no traces of the NeuN neuronal marker in purified tdTomato-positive cells and equal



Galt expression in Dys1AGlast^{+/+} and ^{-/-} mice (Fig. 5d). Importantly, Dys1A expression in Galt-positive astrocytes was abolished in Dys1AGlast^{-/-} mice (Fig. 5e). Compared to Dys1AGlast^{+/+} littermates, Dys1AGlast^{-/-} mice showed the

same GFAP signal, no alteration in astrocytes density, and similar astrocytic morphology (Supplementary Fig. S7). These data demonstrate an inducible deletion of Dys1A in astrocytes, with no gross alterations in astrocytic anatomy.

Fig. 4 **Dys1A** disruption alters vesicular trafficking and Golgi complex morphology in basal ganglia astrocytes. **a** Rab5, **b** Rab9, **c** GALT, and **d** GM130 protein levels in the whole homogenate of GPe from *Dys1A*^{+/+} (*n* = 6), *Dys1A*[±] (*n* = 12) and *Dys1A*^{-/-} (*n* = 8) mice. Protein expression of Rab5, Rab9, GALT and GM130 are reduced in both *Dys1A*[±] and *Dys1A*^{-/-} mice (One-way ANOVA: Rab5: $F_{2,23} = 5.01$; $p = 0.016$; Rab9: $F_{2,23} = 36.24$; $p < 0.0001$; GALT: $F_{2,23} = 27.34$; $p < 0.0001$; GM130: $F_{2,23} = 5.21$; $p = 0.014$). Bar graphs show mean \pm s.e.m. and are expressed as percentages of *Dys1A*^{+/+} mice. Representative immunoblots are shown below each graph (complete immunoblots with loading controls in Supplementary Fig. S4. * $p < 0.05$, ** $p < 0.01$, *** $p < 0.001$ vs *Dys1A*^{+/+} mice, ## $p < 0.01$ vs *Dys1A*[±] mice. **e** Representative transmission electron microscopy (TEM) images of the Golgi Complex (GC, red arrows) from *Dys1A*^{+/+} and *Dys1A*^{-/-} littermates in neuronal and astrocytic cells. Surface density of GC (SvGC/SvCyt) in *Dys1A*^{-/-} was not altered in neurons (*t*-test: $t_{80} = -0.54$, $p = 0.59$), but increased compared with *Dys1A*^{+/+} control mice in astrocytic cells (*t*-test: $t_{68} = -3.38$, $p < 0.001$). ** $p < 0.001$ vs *Dys1A*^{+/+} littermates. **f** Transmission electron microscopy (TEM) images of the Golgi Complex (GC) in neurons and astrocytes in *Dys1*^{+/+} and *Dys1*[±] littermates. Surface density of GC (SvGC/SvCyt) in *Dys1*[±] mice was significantly higher than in *Dys1*^{+/+} littermates (neurons $t_{21} = -2.70$, $p = 0.013$; astrocytes $t_{12} = -4.40$, $p = 0.0009$). * $p < 0.05$, ** $p < 0.001$ vs *Dys1*^{+/+}. **g** Maximum intensity projections of ventral ganglion cells, from *Drosophila* third instar larvae expressing UAS-GalT-GFP to visualize Golgi cisternae, for controls (tubulin-Gal4/+) and UAS-Dysb RNAi. Tissues were labeled with anti α Repo antibody to visualize glial nuclei. Scale bar 20 μ m. **i** Quantification of surface area covered by the GalT-GFP signal in controls (tubulin-Gal4/+) and UAS-Dysb RNAi. The Golgi complex area is expressed as the relative Galt-GFP area (SGalt-GFP)/ROI area (SROI)(7000 μ m²) (unpaired *t*-test; *n* = 10 larvae; * vs Tub/+, **** $p < 0.0001$). On the right TEM images of third instar larvae brain showing the Golgi apparatus of ventral ganglion for the above genotypes. Flies expressing UAS-RNAi *Dysb* ubiquitously showed swelling of largely inflated Golgi cisternae (arrows). Scale bar 500 nm. Relative expression level of *Ddysb* on third instar larvae down-regulated for the *dDys* gene with the driver Tubulin-Gal4 (one-way ANOVA with Tukey's post hoc test. *** $p < 0.0001$). *Dys1A*, but not *Dys1C*, is reduced in the caudate of patients with schizophrenia. **h** Expression of *Dys1A* and *Dys1C* isoforms in postmortem caudate from 22 patients with schizophrenia (Schizophrenia) and 18 matched healthy subjects (Control). No differences were present in non-diagnostic variables (i.e., age, sex, post-mortem interval, pH; Supplementary Fig. S6). Expression of *Dys1A*, normalized by β -actin, is reduced in the caudate of patients with schizophrenia compared to control subjects (*t*-test: $p = 0.02$). *Dys1C* expression is not changed between the two groups (*t*-test: $p = 0.71$). * $p < 0.05$ vs Control. **i** Plotting of β -actin normalized data for *Dys1A* and *Dys1C* for all case-control pairs. Each bar indicates the log₂ transformed ratio of isoform in a schizophrenia case compared to that in its matched control (i.e., the ratio for one case-control pair). Pair-wise analysis of these ratios (Wilcoxon signed-rank test) showed significant difference between schizophrenia cases and their matched controls for *Dys1A* ($W = 154.00$; $p = 0.02$), but not for *Dys1C* ($W = 162.00$; $p = 1.00$). Bar graphs show mean \pm s.e.m.

Dys1A disruption in astrocytes induces motivational and sensorimotor gating deficits

We then tested *Dys1AGlast*^{+/+}, \pm and $-/-$ mice for behavioral phenotypes that were altered by *Dys1A* disruption in all cell types (Fig. 2).

No *Dys1AGlast* genotype effect was evident in exploratory activity (Supplementary Fig. S7). Similar to ubiquitous *Dys1A* disruption, selective *Dys1A* deletion in astrocytes impaired PPI sensorimotor gating abilities (Fig. 5j), while having no effects on startle reactivity or body weight (Supplementary Fig. S7). Furthermore, as observed in *Dys1A* knockout mice (Fig. 2), *Dys1AGlast*[±] and $-/-$ mice showed reduced motivation to work for a rewarding stimulus (Fig. 5k), while no *Dys1AGlast* genotype effects were evident on the acquisition of this operant task (Supplementary Fig. S7).

These results indicate that astrocytic *Dys1A* is involved in the modulation of sensorimotor gating and motivational processes.

Dys1A disruption in astrocytes alters basal ganglia dopamine homeostasis and increases D2 in astrocytes

We then investigated the effects of astrocytic *Dys1A* on dopaminergic signaling in basal ganglia.

Like ubiquitous *Dys1A* disruption (Fig. 3), astrocytic *Dys1A* disruption reduced dopamine levels primarily in GPe and marginally in STR (Fig. 5h). No effects were observed in PFC (Supplementary Fig. S7). No *Dys1AGlast* effect was evident for DOPAC levels (Fig. 5i), while HVA levels were reduced in *Dys1AGlast* knockout mice compared with wild-type littermates in both STR and GPe (Fig. 5j). These findings demonstrate that disruption of *Dys1A* in astrocytes reduce dopamine levels, primarily in GPe.

We next assessed the impact of *Dys1A* disruption in astrocytes on the expression of genes involved in dopaminergic signaling and metabolism in purified astrocytes isolated from the basal ganglia region (Fig. 5k). We found detectable levels of mRNA expression for dopamine receptors D1, D2, and D3, for the plasma membrane dopamine (DAT) and organic cation 3 (OCT3) transporters, and the metabolic enzyme monoamine oxidase type B (MAOB (Supplementary Fig. S7). No detectable signals were evident for tyrosine hydroxylase (TH), the rate-limiting enzyme in

dopamine synthesis, and for the vesicular monoamine transporter VMAT2 that has been implicated in astrocytic dopamine homeostasis in PFC [21]. We excluded neuronal contamination, as no detectable levels of the NeuN marker were found (Supplementary Fig. S7).

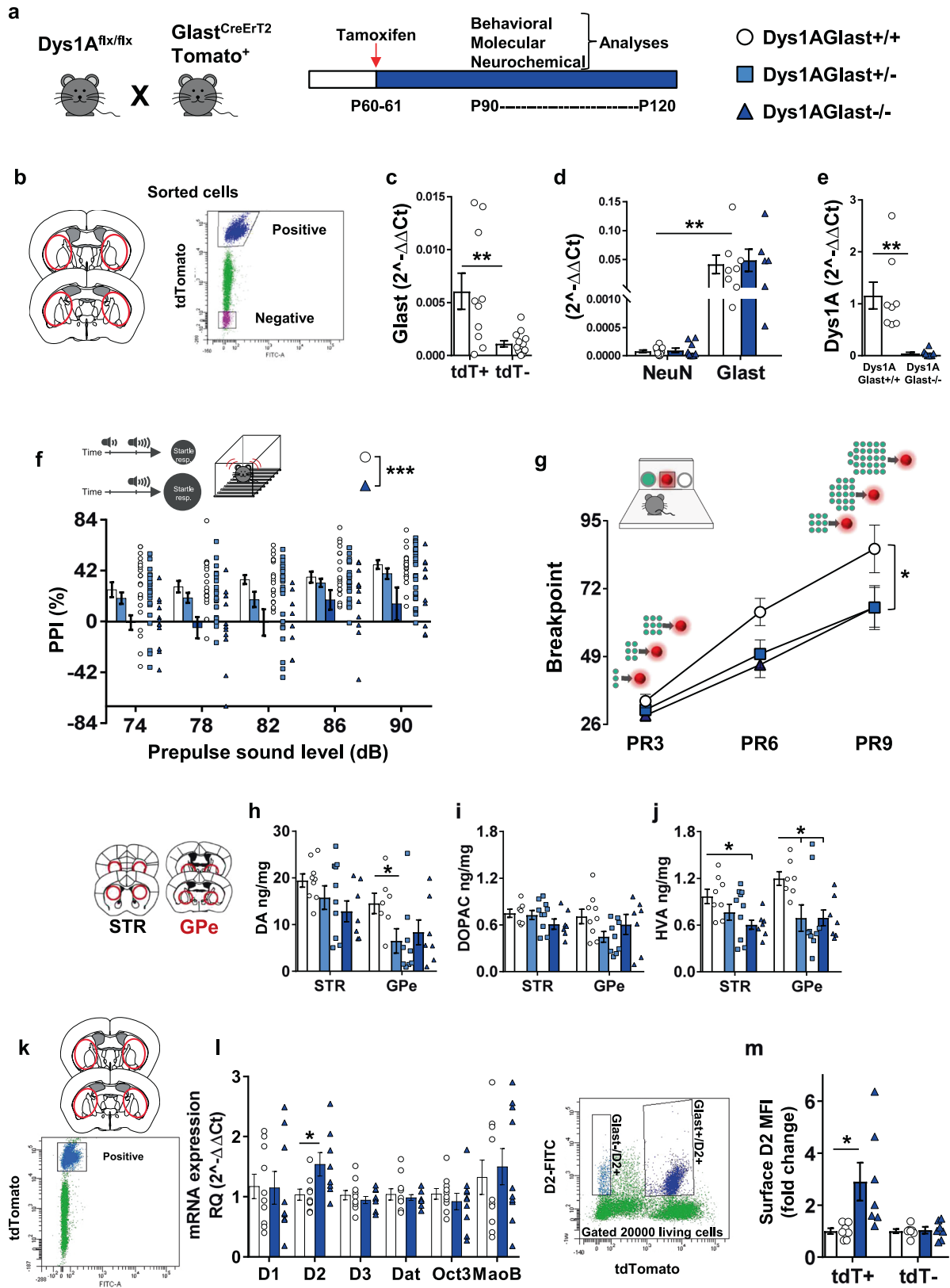
Among all these markers, only astrocytic expression of dopamine D2 receptor was altered, with *Dys1AGlast*^{-/-} mice showing higher D2 mRNA level than *Dys1AGlast*^{+/+} (Fig. 5l). This is in accordance with and extends the effects of ubiquitous disruption of *Dys1* on expression of D2 receptors in basal ganglia (Supplementary Fig. S3). Similarly, in *Drosophila*, ubiquitous, glia- or neuron-specific disruption of *dDys* equivalently increased D2 expression (Supplementary Fig. S6). Notably, we confirmed by flow cytometry an increased protein expression of D2 receptors on the surface of *Glast*/tdTomato positive astrocytes from *Dys1AGlast*^{-/-} mice compared with *Dys1AGlast*^{+/+} (Fig. 5m). In these same mice, no genotype-dependent differences in D2 protein expression were evident on *Glast*/tdTomato negative cells (Fig. 5m), confirming the upregulation of D2 receptor in astrocytes upon *Dys1A* disruption, without any compensatory D2 perturbation in other cells.

These data suggest that *Dys1A*-dependent behavioral and dopaminergic alterations might relate to increased astrocytic D2 mechanisms.

DISCUSSION

In this study, we reveal *Dys1A* participation in astrocytic functioning with a bias toward basal ganglia-related behavioral and dopaminergic phenotypes, with implications for schizophrenia. Specifically, the *Dys1A* isoform that is reduced in the caudate of patients with schizophrenia, is the only *Dys1* isoform expressed by astrocytes. Disruption of *Dys1A* ubiquitously or in astrocytes is associated with alterations of basal ganglia-dependent phenotypes.

Dys1A affected basal ganglia dopaminergic and behavioral functions, while sparing cortex-related phenotypes. In contrast to *Dys1A*, the expression of *Dys1C* increases during cortical development (Fig. 1), and it is selectively reduced in PFC of patients with schizophrenia [15]. This suggests that well-established *Dys1*-



dependent dopaminergic and behavioral alterations at the cortical level [1, 3, 14, 64] may be more related to neuronal Dys1C. Moreover, recent evidence suggests that astrocytic mechanisms related to dopamine signaling might differ between PFC [21],

basal ganglia GPe [20], and NAcc [22]. In particular, in the PFC the astroglial vesicular monoamine transporter 2 (VMAT2) has a major involvement on dopaminergic signaling [21], within the GPe D2 but not D1 receptors can modulate astrocytic activity [20], while

Fig. 5 Dys1A disruption in astrocytes induce sensorimotor gating and motivational deficits, decrease basal ganglia dopamine, and increase astrocytic D2 receptors. **a** Experimental design and timeline to generate reduction (\pm) or absence ($-/-$) of Dys1A in astrocytes of adult mice subsequently subjected to molecular and behavioral evaluation. Dys1A floxed mice were bred with conditional $\text{Glast}^{\text{CreERT2}}\text{Tomato}^+$ mice, and offspring were treated with tamoxifen at post-natal days 60–61 to then be tested between post-natal days 90–120. **b** Gating strategy to FACS-sorted astrocytes for subsequent RT-qPCR analyses. **c** Relative mRNA expression of *Glast* assessed by RT-qPCR in tdTomato-positive (tdT+) and tdTomato-negative (tdT-) cells sorted from the basal ganglia of Dys1AGlast+/+ (n10) and Dys1AGlast-/- (n13) mice. tdT+ cells show increased expression of *Glast* compared to tdT- cells (*t*-test: $t = 3.25$, $df = 21$, $p < 0.005$). $**p < 0.005$ tdT+ vs tdT- cells. **d** Relative mRNA expression of *NeuN* and *Glast* assessed by RT-qPCR in tdTomato-positive cells sorted from the basal ganglia of Dys1AGlast+/+ (n10) and Dys1AGlast-/- (n10) mice. tdTomato-positive cells show an equal expression of *Glast* in Dys1AGlast+/+ and Dys1AGlast-/- mice (Two-way ANOVA; genotype effect: $F_{1,12} = 0.084$; $p = 0.78$), but no detectable levels of *NeuN* (Two-way ANOVA; gene expression: $F_{1,12} = 13.16$; $p = 0.003$). $**p < 0.005$ *Glast* vs *NeuN*. Expression levels were normalized by *Gapdh* expression. **e** Relative mRNA expression of the *Dys1A* isoform assessed by RT-qPCR in tdTomato-positive cells sorted through FACS from the basal ganglia of Dys1AGlast+/+ (n8) and Dys1AGlast-/- (n8) mice, showing the abolishment of *Dys1A* expression from *Glast*-positive astrocytes in the latter group (One-way ANOVA; $F_{1,14} = 18.32$; $p = 0.0008$). $**p < 0.005$ vs Dys1AGlast+/+. Expression levels are normalized by *Gapdh* expression. Data shown as fold-change compared with Dys1AGlast+/+ control mice. **f** Percent pre-pulse inhibition (PPI) of the 120 dB acoustic startle response displayed by Dys1AGlast+/+ (n21), Dys1AGlast \pm (n24), and Dys1AGlast-/- (n13) littermates. Dys1AGlast-/- have reduced PPI compared to Dys1AGlast+/+ mice (Two-way repeated measure ANOVA; genotype effect: $F_{2,54} = 8.59$, $p = 0.0006$). $***p < 0.0005$ vs Dys1AGlast+/+. **g** Breakpoint during a food-driven operant behavior test with increasing progressive ratio (PR) displayed by Dys1AGlast+/+ (n15), Dys1AGlast \pm (n15), and Dys1AGlast-/- (n9) littermates. Both Dys1AGlast \pm and Dys1AGlast-/- mice showed lower breakpoints than Dys1AGlast+/+ mice (Two-way repeated measure ANOVA; genotype effect: $F_{2,36} = 4.35$; $p = 0.020$). $*p < 0.05$ vs Dys1AGlast+/+. **h** Dopamine (DA), **(i)** DOPAC, and **(j)** HVA content by HPLC analyses, expressed as ng/mg of dissected STR or GPe tissues displayed by Dys1AGlast+/+ (n9), Dys1AGlast \pm (n10), and Dys1AGlast-/- (n7) littermates. In the STR, Dys1AGlast-/- had reduced HVA levels (One-way ANOVA: $F_{2,22} = 3.52$; $p = 0.04$), but no alterations in DA (One-way ANOVA: $F_{2,23} = 2.15$; $p = 0.14$), and DOPAC levels (One-way ANOVA: $F_{2,21} = 1.40$; $p = 0.27$), compared to Dys1AGlast+/+ mice. In the GPe, Dys1AGlast knockout mice had reduced DA (One-way ANOVA: $F_{2,20} = 4.85$; $p = 0.02$; by Bonferroni correction only \pm vs $+/+$ $p < 0.05$), and HVA levels (One-way ANOVA: $F_{2,20} = 4.46$; $p = 0.02$), but no alterations in DOPAC (One-way ANOVA: $F_{2,22} = 2.08$; $p = 0.15$), compared to Dys1AGlast+/+ mice. $*p < 0.05$ vs Dys1AGlast+/+ mice. **k** Gating strategy to FACS-sorted astrocytes from STR + GPe regions for subsequent RT-qPCR analyses for astrocytic dopaminergic markers. **l** Relative mRNA expression of dopamine receptors (D1, D2, D3), *Dat*, *Oct3* and *MaoB*, assessed by RT-qPCR in tdTomato-positive cells sorted from basal ganglia of Dys1AGlast+/+ (n10) and Dys1AGlast-/- (n10) littermates, revealing an increased astrocytic D2 receptor expression in Dys1AGlast-/- mice (*t*-tests: $t_{17} = -2.42$, $p = 0.029$), and no genotype effect for the other assessed markers (D1: $t_{17} = 0.07$, $p = 0.95$; D3: $t_{17} = 0.81$, $p = 0.43$; *Dat*: $t_{17} = 0.50$, $p = 0.62$; *Oct3*: $t_{17} = 0.76$, $p = 0.46$; *MaoB*: $t_{17} = -0.00$, $p = 1.00$). Data shown as fold-change compared with Dys1AGlast+/+ control mice. $*p < 0.05$ vs Dys1AGlast+/+ mice. **m** Flow cytometry gating strategy and surface D2 receptor protein expression quantification in tdTomato-positive (tdT+) and negative (tdT-) cells from the basal ganglia of Dys1AGlast+/+ (n7) and Dys1AGlast-/- (n7) expressed as mean fluorescence intensity (MFI), revealing increased astrocytic surface D2 expression in Dys1AGlast-/- mice compared to Dys1AGlast+/+ only in tdTomato-positive cells (Two-way ANOVA: genotype*cell-type interaction: $F_{1,12} = 5.71$; $p = 0.03$). Data shown as fold-change compared with Dys1AGlast+/+ control mice. $*p < 0.01$ Dys1AGlast-/- tdT+ vs all other groups. Bar and line graphs show mean \pm s.e.m.

viceversa in the NAcc D1 but not D2 receptors can modulate astrocyte Ca^{2+} responses to dopamine [22]. Thus, *Dys1A* modulation of astrocytic functioning and D2 receptor expression may constitute another biological substrate explaining its bias toward basal ganglia dopamine and behavioral alterations. Our findings also suggest astrocytes as a player in the dopaminergic cortical/basal ganglia dichotomy and related behavioral abnormalities consistently reported in schizophrenia [65, 66]. Astrocytic *Dys1A* could contribute to striatal-related behavioral abnormalities and basal ganglia D2 upregulation found in schizophrenia [67]. Obviously, *Dys1A* is expected to interact with several other factors that can finally bring to the complex behavioral and dopaminergic phenotypes evident in schizophrenia, and these interactions will need dedicated studies. The differential control exerted by astrocytic *Dys1A* on cortical and basal ganglia dopamine-related behaviors adds to increasing evidence for heterogeneous astrocyte-mediated processes across different brain regions [68–70]. However, despite we selectively deleted *Dys1A* and astrocytic *Dys1A*, here we targeted all the brain. Thus, future studies with region specific manipulations are needed to clarify the mechanisms by which astrocytic *Dys1A* modulates behaviors and related dopaminergic circuits within the basal ganglia.

We reveal that disruption of *Dys1A* ubiquitously or in astrocytes have evident effects on motivated behavior and sensorimotor gating. *Dys1A* reduction decreased dopamine content and increased levels of D2 receptors in basal ganglia, and this was associated with reduced motivation to work for food reward and sensorimotor gating deficits. This agrees with compelling evidence that dopamine levels in basal ganglia are proportionally related to motivational behavior [71]. Similarly, striatal overexpression of D2 receptors by the *CaMKII* promoter [67], which is also present in astrocytes [72], reduced motivation [54]. In

contrast, *Dys1A* disruption did not alter gross motor functions and locomotor responses to amphetamine, despite altering dopamine tissue and D2 levels within the GPe, and partially in STR. Similarly, even *Dys1* deletion altered STR dopamine levels while sparing locomotor responses to amphetamine [46, 58]. The reason for this lack of altered responses to amphetamine would require more dedicated experimentation, but based on our new findings, it could be related to *Dys1A* alteration of astrocytic D2 signaling, which have been reported to influence STR GABAergic and dopaminergic release [73]. Noteworthy, we found the largest changes by *Dys1A* not in STR, but in the GPe. Historically, GPe has also been implicated in movement control [74]. However, in agreement with our findings, recent studies show GPe involvement in motivational and sensorimotor gating processes [75–78]. Moreover, dopaminergic manipulations within GPe may not alter motor functions [75, 78, 79], and D2 receptors do not contribute to amphetamine-evoked astrocytic responses [22]. Instead, astrocyte-dopamine interactions within VTA-NAcc dopamine/D1 pathways are involved in locomotor processes [22]. Overall, our data show that *Dys1A* regulates astrocytes, motivational and sensorimotor gating processes involving dopamine/D2-dependent alterations in GPe. Astrocytic *Dys1A* represents therefore a potential cell-specific target for the treatment of motivational and other neuropsychiatric disorders associated with disrupted dopamine/D2 signaling.

In agreement with previous studies on *Dys1* [17, 57, 58], we report that also *Dys1A* reduction can disrupt vesicular trafficking. *Dys1*-dependent disruptions of vesicular trafficking cause an increased presence on the neuronal surface of those receptors that normally rely on internalization/degradation processes [17, 57, 58]. In particular, dopamine D2-like receptors, in contrast to D1-like, follow these intracellular pathways [80, 81], and are

consequently influenced by Dys1 disruption [3, 17, 58]. Accordingly, we found that Dys1A disruption altered the surface expression of D2 receptors. However, in agreement with the fact that Dys1A seemed to alter vesicular inclusions mainly in astrocytes and not in neurons, it is tempting to speculate that D2 overexpression would be present mostly on the surface of astrocytes, as we confirmed when deleting Dys1A only in astrocytes. This D2 astrocytic overexpression might then alter the GABAergic inhibitory tone of striatal dopamine, as previously reported [73, 82]. In agreement, Dys1A depletion only in astrocytes reduced dopamine levels in basal ganglia (especially GPe). Furthermore, conditions of reduced dopamine in GPe and STR are associated with increased astrocytic activity and augmented astrocyte-related GABA inhibition of dopamine release [20, 73]. Viceversa, inhibiting astrocytes in STR can increase dopamine levels [83]. The conundrum would be why Dys1A, which is also expressed in neurons, is influencing more astrocytes. Noteworthy, our developmental profiling reveals that in adult brains, expression of Dys1A is lower than Dys1C. Moreover, we found that in neurons expression of Dys1C is higher than Dys1A. Thus, Dys1A might have a more marginal function in adult neuronal cells. Furthermore, the greater neuronal prominence of Dys1C might compensate the Dys1A disruption. In contrast, as astrocytes express only the Dys1A isoform, its disruption would generate more consistent alterations, at least in our condition which avoided developmental effects as astrocytic Dys1A was deleted only in adulthood. The defective morphology of Golgi apparatus, observed at both structural and molecular levels, likely contributes to the impaired secretory traffic or simply reflect altered astrocytic homeostasis dependent from Dys1A disruption. Moreover, the intracellular trafficking markers addressed in our study have been reported to participate in astrocytic functioning and, more importantly, in the regulation of intracellular Ca^{2+} in these cells [84–86]. This might then be related to Dys1-dependent alterations of astrocytic Ca^{2+} signal dynamics that we observed, even if future studies should address how selective Dys1A deletion in astrocytes could influence their Ca^{2+} transients. Overall, our findings indicate a link between Dys1A and astrocyte-related dopaminergic signaling, with an impact on clinically relevant behavioral abnormalities. More focused in vitro cellular studies are needed to elucidate the exact intracellular mechanisms linking Dys1A to astrocytic functioning.

In summary, we uncovered a previously unexplored role for the Dys1A isoform in the modulation of astrocytic activity and dopamine/D2 signaling that is prevalently evident in basal ganglia, with implications for motivational and sensorimotor gating abilities relevant to schizophrenia. These findings further indicate astrocytes involvement in dopamine-related behavioral dysfunctions in psychiatric disorders. Indeed, our findings point to basal ganglia astrocytes as a promising target for the treatment of dopamine dysfunctions in schizophrenia.

REFERENCES

- Leggio GM, Torrisi SA, Mastrogiacomo R, Mauro D, Chisari M, Devroye C, et al. The epistatic interaction between the dopamine D3 receptor and dysbindin-1 modulates higher-order cognitive functions in mice and humans. *Mol Psychiatry*. 2021;26:1272–85. <https://doi.org/10.1038/s41380-019-0511-4>. Epub 2019 Sep 6.
- Savage JE, Jansen PR, Stringer S, Watanabe K, Bryois J, de Leeuw CA, et al. Genome-wide association meta-analysis in 269,867 individuals identifies new genetic and functional links to intelligence. *Nat Genet*. 2018;50:912–9.
- Scheggia D, Mastrogiacomo R, Mereu M, Sannino S, Straub RE, Armando M, et al. Variations in Dysbindin-1 are associated with cognitive response to antipsychotic drug treatment. *Nat Commun*. 2018;9:2265.
- Waddington JL, Zhen X, O'Tuathaigh CMP. Developmental Genes and Regulatory Proteins, Domains of Cognitive Impairment in Schizophrenia Spectrum Psychosis and Implications for Antipsychotic Drug Discovery: The Example of Dysbindin-1 Isoforms and Beyond. *Front Pharm*. 2019;10:1638.

- Straub RE, MacLean CJ, O'Neill FA, Burke J, Murphy B, Duke F, et al. A potential vulnerability locus for schizophrenia on chromosome 6p24-22: evidence for genetic heterogeneity. *Nat Genet*. 1995;11:287–93.
- Talbot K, Ong WY, Blake DJ, Tang J, Louneva N, Carlson GC et al. Dysbindin-1 and Its Protein Family. In: Javitt DC, Kantrowitz J, editors. *Handbook of Neurochemistry and Molecular Neurobiology*, 3rd edn. New York:Springer Science;2009. p. 107–241.
- Marshall CR, Howrigan DP, Merico D, Thiruvahindrapuram B, Wu W, Greer DS, et al. Contribution of copy number variants to schizophrenia from a genome-wide study of 41,321 subjects. *Nat Genet*. 2017;49:27–35.
- Pae CU, Drago A, Kim JJ, Patkar AA, Jun TY, Lee C, et al. DTNBP1 haplotype influences baseline assessment scores of schizophrenic in-patients. *Neurosci Lett*. 2008;440:150–4.
- Bray NJ, Preece A, Williams NM, Moskvina V, Buckland PR, Owen MJ, et al. Haplotypes at the dystrobrevin binding protein 1 (DTNBP1) gene locus mediate risk for schizophrenia through reduced DTNBP1 expression. *Hum Mol Genet*. 2005;14:1947–54.
- Straub RE, Jiang Y, MacLean CJ, Ma Y, Webb BT, Myakishev MV, et al. Genetic variation in the 6p22.3 gene DTNBP1, the human ortholog of the mouse dysbindin gene, is associated with schizophrenia. *Am J Hum Genet*. 2002;71:337–48.
- Voisey J, Swagell CD, Hughes IP, Lawford BR, Young RM, Morris CP. Analysis of HapMap tag-SNPs in dysbindin (DTNBP1) reveals evidence of consistent association with schizophrenia. *Eur Psychiatry*. 2010;25:314–9.
- Talbot K, Eidem WL, Tinsley CL, Benson MA, Thompson EW, Smith RJ, et al. Dysbindin-1 is reduced in intrinsic, glutamatergic terminals of the hippocampal formation in schizophrenia. *J Clin Investig*. 2004;113:1353–63.
- Weickert CS, Straub RE, McClintock BW, Matsumoto M, Hashimoto R, Hyde TM, et al. Human dysbindin (DTNBP1) gene expression in normal brain and in schizophrenic prefrontal cortex and midbrain. *Arch Gen Psychiatry*. 2004;61:544–55.
- Papaleo F, Weinberger DR. Dysbindin and Schizophrenia: it's dopamine and glutamate all over again. *Biol Psychiatry*. 2011;69:2–4.
- Tang J, LeGros RP, Louneva N, Yeh L, Cohen JW, Hahn CG, et al. Dysbindin-1 in dorsolateral prefrontal cortex of schizophrenia cases is reduced in an isoform-specific manner unrelated to dysbindin-1 mRNA expression. *Hum Mol Genet*. 2009;18:3851–63.
- Wentzel C, Delvendahl I, Sydlik S, Georgiev O, Muller M. Dysbindin links presynaptic proteasome function to homeostatic recruitment of low release probability vesicles. *Nat Commun*. 2018;9:267.
- Ji Y, Yang F, Papaleo F, Wang HX, Gao WJ, Weinberger DR, et al. Role of dysbindin in dopamine receptor trafficking and cortical GABA function. *Proc Natl Acad Sci USA*. 2009;106:19593–8.
- Shao L, Shuai Y, Wang J, Feng S, Lu B, Li Z, et al. Schizophrenia susceptibility gene dysbindin regulates glutamatergic and dopaminergic functions via distinctive mechanisms in *Drosophila*. *Proc Natl Acad Sci USA*. 2011;108:18831–6.
- Shao W, Zhang SZ, Tang M, Zhang XH, Zhou Z, Yin YQ, et al. Suppression of neuroinflammation by astrocytic dopamine D2 receptors via alphaB-crystallin. *Nature*. 2013;494:90–4.
- Cui Q, Pitt JE, Pamukcu A, Poulin JF, Mabrouk OS, Fiske MP, et al. Blunted mGluR Activation Disinhibits Striatopallidal Transmission in Parkinsonian Mice. *Cell Rep*. 2016;17:2431–44.
- Petrelli F, Dall'è G, Pucci L, Cali C, Zehnder T, Sultan S, et al. Dysfunction of homeostatic control of dopamine by astrocytes in the developing prefrontal cortex leads to cognitive impairments. *Mol Psychiatry*. 2020;25:732–49. <https://doi.org/10.1038/s41380-018-0226-y>.
- Corkrum M, Covelo A, Lines J, Bellocchio L, Pisansky M, Loke K, et al. Dopamine-Evoked Synaptic Regulation in the Nucleus Accumbens Requires Astrocyte Activity. *Neuron*. 2020;105:1036–47.e5. <https://doi.org/10.1016/j.neuron.2019.12.026>. Epub 2020 Jan 15.
- Talbot K, Louneva N, Cohen JW, Kazi H, Blake DJ, Arnold SE. Synaptic dysbindin-1 reductions in schizophrenia occur in an isoform-specific manner indicating their subsynaptic location. *PLoS ONE*. 2011;6:e16886.
- Larimore J, Zlatic SA, Gokhale A, Tornieri K, Singleton KS, Mullin AP, et al. Mutations in the BLOC-1 subunits dysbindin and muted generate divergent and dosage-dependent phenotypes. *J Biol Chem*. 2014;289:14291–300.
- Yuan Y, Wang H, Wei Z, Li W. Impaired autophagy in hilar mossy cells of the dentate gyrus and its implication in schizophrenia. *J Genet Genom*. 2015;42:1–8.
- Petit EJ, Michalak Z, Cox R, O'Tuathaigh CM, Clarke N, Tighe O, et al. Dysregulation of Specialized Delay/Interference-Dependent Working Memory Following Loss of Dysbindin-1A in Schizophrenia-Related Phenotypes. *Neuropsychopharmacology*. 2017;42:1349–60.
- Mori T, Tanaka K, Buffo A, Wurst W, Kuhn R, Gotz M. Inducible gene deletion in astroglia and radial glia—a valuable tool for functional and lineage analysis. *Glia*. 2006;54:21–34.
- Scheggia D, Zamberletti E, Realini N, Mereu M, Contarini G, Ferretti V, et al. Remote memories are enhanced by COMT activity through dysregulation of the endocannabinoid system in the prefrontal cortex. *Mol Psychiatry*. 2018;23:1040–50.

29. Paxinos G, Franklin KBJ. The mouse brain in stereotaxic coordinates. Amsterdam: Elsevier Academic Press; 2004.
30. Dugue GP, Dumoulin A, Triller A, Dieudonne S. Target-dependent use of co-released inhibitory transmitters at central synapses. *J Neurosci*. 2005;25:6490–8.
31. Srinivasan R, Huang BS, Venugopal S, Johnston AD, Chai H, Zeng H, et al. Ca(2+) signaling in astrocytes from *lpr32(-/-)* mice in brain slices and during startle responses in vivo. *Nat Neurosci*. 2015;18:708–17.
32. Mariotti L, Losi G, Lia A, Melone M, Chiavegato A, Gomez-Gonzalo M, et al. Interneuron-specific signaling evokes distinctive somatostatin-mediated responses in adult cortical astrocytes. *Nat Commun*. 2018;9:82.
33. Caffino L, Verheij MMM, Roversi K, Targa G, Mottarlini F, Popik P, et al. Hypersensitivity to amphetamine's psychomotor and reinforcing effects in serotonin transporter knockout rats: Glutamate in the nucleus accumbens. *Br J Pharm*. 2020;177:4532–47.
34. Huang H, Michetti C, Busnelli M, Manago F, Sannino S, Scheggia D, et al. Chronic and acute intranasal oxytocin produce divergent social effects in mice. *Neuropsychopharmacology*. 2014;39:1102–14.
35. Scheggia D, Bebensee A, Weinberger DR, Papaleo F. The ultimate intra-/extra-dimensional attentional set-shifting task for mice. *Biol Psychiatry*. 2014;75:660–70.
36. Manago F, Mereu M, Mastwal S, Mastrogiacomo R, Scheggia D, Emanuele M, et al. Genetic Disruption of *Arc/Arg3.1* in Mice Causes Alterations in Dopamine and Neurobehavioral Phenotypes Related to Schizophrenia. *Cell Rep*. 2016;16:2116–28.
37. Papaleo F, Kieffer BL, Tabarin A, Contarino A. Decreased motivation to eat in mu-opioid receptor-deficient mice. *Eur J Neurosci*. 2007;25:3398–405.
38. Polishchuk RS, Mironov AA. Correlative video light/electron microscopy. *Curr Protoc Cell Biol*. 2001;Chapter 4:Unit 4.8. <https://doi.org/10.1002/0471143030.cb0408s11>.
39. Luskin MB, Parnavelas JG, Barfield JA. Neurons, astrocytes, and oligodendrocytes of the rat cerebral cortex originate from separate progenitor cells: an ultrastructural analysis of clonally related cells. *J Neurosci*. 1993;13:1730–50.
40. Nahirney PC, Tremblay ME. Brain ultrastructure: putting the pieces together. *Front Cell Dev Biol*. 2021;9:629503.
41. Orso G, Pendin D, Liu S, Tosetto J, Moss TJ, Faust JE, et al. Homotypic fusion of ER membranes requires the dynamin-like GTPase atlastin. *Nature*. 2009;460:978–83.
42. De Filippis C, Napoli B, Rigon L, Guarato G, Bauer R, Tomanin R et al. *Drosophila* D-idea Reduction Mimics Mucopolysaccharidosis Type I Disease-Related Phenotypes. *Cells* 2021;11:129. <https://doi.org/10.3390/cells11010129>.
43. Scheggia D, Manago F, Maltese F, Bruni S, Nigro M, Dautan D, et al. Somatostatin interneurons in the prefrontal cortex control affective state discrimination in mice. *Nat Neurosci*. 2020;23:47–60.
44. Zamanian JL, Xu L, Foo LC, Nouri N, Zhou L, Giffard RG, et al. Genomic analysis of reactive astrogliosis. *J Neurosci*. 2012;32:6391–410.
45. Ferretti V, Maltese F, Contarini G, Nigro M, Bonavia A, Huang H, et al. Oxytocin Signaling in the Central Amygdala Modulates Emotion Discrimination in Mice. *Curr Biol*. 2019;29:1938–53 e1936.
46. Papaleo F, Yang F, Garcia S, Chen J, Lu B, Crawley JN, et al. Dysbindin-1 modulates prefrontal cortical activity and schizophrenia-like behaviors via dopamine/D2 pathways. *Mol Psychiatry*. 2012;17:85–98.
47. Feng YQ, Zhou ZY, He X, Wang H, Guo XL, Hao CJ, et al. Dysbindin deficiency in sandy mice causes reduction of *snappin* and displays behaviors related to schizophrenia. *Schizophrenia Res*. 2008;106:218–28.
48. Hattori S, Murotani T, Matsuzaki S, Ishizuka T, Kumamoto N, Takeda M, et al. Behavioral abnormalities and dopamine reductions in *sdv* mutant mice with a deletion in *Dtnbp1*, a susceptibility gene for schizophrenia. *Biochem Biophys Res Commun*. 2008;373:298–302.
49. Robbins TW. Shifting and stopping: fronto-striatal substrates, neurochemical modulation and clinical implications. *Philos Trans R Soc Lond*. 2007;362:917–32.
50. Clarke HF, Hill GJ, Robbins TW, Roberts AC. Dopamine, but not serotonin, regulates reversal learning in the marmoset caudate nucleus. *J Neurosci*. 2011;31:4290–7.
51. Doherty JM, Masten VL, Powell SB, Ralph RJ, Klamer D, Low MJ, et al. Contributions of dopamine D1, D2, and D3 receptor subtypes to the disruptive effects of cocaine on prepulse inhibition in mice. *Neuropsychopharmacology*. 2008;33:2648–56.
52. Koch M. The neurobiology of startle. *Prog Neurobiol*. 1999;59:107–28.
53. Plappert CF, Pilz PK, Schnitzler HU. Factors governing prepulse inhibition and prepulse facilitation of the acoustic startle response in mice. *Behav Brain Res*. 2004;152:403–12.
54. Drew MR, Simpson EH, Kellendonk C, Herzberg WG, Lipatova O, Fairhurst S, et al. Transient overexpression of striatal D2 receptors impairs operant motivation and interval timing. *J Neurosci*. 2007;27:7731–9.
55. Ward RD, Kellendonk C, Kandel ER, Balsam PD. Timing as a window on cognition in schizophrenia. *Neuropharmacology*. 2012;62:1175–81. <https://doi.org/10.1016/j.neuropharm.2011.04.014>. Epub 2011 Apr 21.
56. Ward RD, Kellendonk C, Simpson EH, Lipatova O, Drew MR, Fairhurst S, et al. Impaired timing precision produced by striatal D2 receptor overexpression is mediated by cognitive and motivational deficits. *Behav Neurosci*. 2009;123:720–30.
57. Marley A, von Zastrow M. Dysbindin promotes the post-endocytic sorting of G protein-coupled receptors to lysosomes. *PLoS ONE*. 2010;5:e9325.
58. Leggio GM, Torrisi SA, Mastrogiacomo R, Mauro D, Chisari M, Devroye C, et al. The epistatic interaction between the dopamine D3 receptor and dysbindin-1 modulates higher-order cognitive functions in mice and humans. *Mol Psychiatry*. 2021;26:1272–85.
59. Bucci C, Parton RG, Mather IH, Stunnenberg H, Simons K, Hoflack B, et al. The small GTPase *rab5* functions as a regulatory factor in the early endocytic pathway. *Cell*. 1992;70:715–28.
60. Soldati T, Rancano C, Geissler H, Pfeffer SR. Rab7 and Rab9 are recruited onto late endosomes by biochemically distinguishable processes. *J Biol Chem*. 1995;270:25541–8.
61. Liu X, Cheng C, Shao B, Wu X, Ji Y, Lu X, et al. The functional interaction between CDK11p58 and beta-1,4-galactosyltransferase I involved in astrocyte activation caused by lipopolysaccharide. *Inflammation*. 2012;35:1365–77.
62. Nakamura N, Rabouille C, Watson R, Nilsson T, Hui N, Slusarewicz P, et al. Characterization of a cis-Golgi matrix protein, GM130. *J Cell Biol*. 1995;131:1715–26.
63. Santello M, Toni N, Volterra A. Astrocyte function from information processing to cognition and cognitive impairment. *Nat Neurosci*. 2019;22:154–66.
64. Papaleo F, Burdick MC, Callicott JH, Weinberger DR. Epistatic interaction between *COMT* and *DTNBP1* modulates prefrontal function in mice and in humans. *Mol Psychiatry*. 2014;19:311–6.
65. Weinstein JJ, Chohan MO, Slifstein M, Kegeles LS, Moore H, Abi-Dargham A. Pathway-Specific Dopamine Abnormalities in Schizophrenia. *Biol Psychiatry*. 2017;81:31–42.
66. Winterer G, Weinberger DR. Genes, dopamine and cortical signal-to-noise ratio in schizophrenia. *Trends Neurosci*. 2004;27:683–90.
67. Simpson EH, Kellendonk C. Insights About Striatal Circuit Function and Schizophrenia From a Mouse Model of Dopamine D2 Receptor Upregulation. *Biol Psychiatry*. 2017;81:21–30.
68. Chai H, Diaz-Castro B, Shigetomi E, Monte E, Oceau JC, Yu X, et al. Neural Circuit-Specialized Astrocytes: Transcriptomic, Proteomic, Morphological, and Functional Evidence. *Neuron*. 2017;95:531–49 e539.
69. Ben Haim L, Rowitch DH. Functional diversity of astrocytes in neural circuit regulation. *Nat Rev Neurosci*. 2017;18:31–41.
70. Huang AY, Woo J, Sardar D, Lozzi B, Bosquez Huerta NA, Lin CJ, et al. Region-Specific Transcriptional Control of Astrocyte Function Oversees Local Circuit Activities. *Neuron*. 2020;106:992–1008 e1009.
71. Mohebi A, Pettibone JR, Hamid AA, Wong JT, Vinson LT, Patriarchi T, et al. Dissociable dopamine dynamics for learning and motivation. *Nature*. 2019;570:65–70.
72. Takeuchi Y, Yamamoto H, Fukunaga K, Miyakawa T, Miyamoto E. Identification of the isoforms of Ca(2+)/Calmodulin-dependent protein kinase II in rat astrocytes and their subcellular localization. *J Neurochem*. 2000;74:2557–67.
73. Roberts BM, Doig NM, Brimblecombe KR, Lopes EF, Siddorn RE, Threlfell S, et al. GABA uptake transporters support dopamine release in dorsal striatum with maladaptive downregulation in a parkinsonism model. *Nat Commun*. 2020;11:4958.
74. Gittis AH, Berke JD, Bevan MD, Chan CS, Mallet N, Morrow MM, et al. New roles for the external globus pallidus in basal ganglia circuits and behavior. *J Neurosci*. 2014;34:15178–83.
75. Carvalho Poyraz F, Holzner E, Bailey MR, Meszaros J, Kenney L, Kheirbek MA, et al. Decreasing Striatopallidal Pathway Function Enhances Motivation by Energizing the Initiation of Goal-Directed Action. *J Neurosci*. 2016;36:5988–6001.
76. Fiore VG, Nolte T, Rigoli F, Smittenaar P, Gu X, Dolan RJ. Value encoding in the globus pallidus: fMRI reveals an interaction effect between reward and dopamine drive. *Neuroimage*. 2018;173:249–57.
77. Miller JM, Vorel SR, Tranchesi AJ, Kenny ET, Mazzoni P, van Gorp WG, et al. Anhedonia after a selective bilateral lesion of the globus pallidus. *Am J Psychiatry*. 2006;163:786–8.
78. Sotoyama H, Zheng Y, Iwakura Y, Mizuno M, Aizawa M, Shcherbakova K, et al. Pallidal hyperdopaminergic innervation underlying D2 receptor-dependent behavioral deficits in the schizophrenia animal model established by EGF. *PLoS ONE*. 2011;6:e25831.
79. Avila G, Picazo O, Chuc-Meza E, Garcia-Ramirez M. Reduction of dopaminergic transmission in the globus pallidus increases anxiety-like behavior without altering motor activity. *Behav Brain Res*. 2020;386:112589.
80. Bartlett SE, Enquist J, Hopf FW, Lee JH, Gladher F, Kharaznia V, et al. Dopamine responsiveness is regulated by targeted sorting of D2 receptors. *Proc Natl Acad Sci USA*. 2005;102:11521–6.

81. Thompson D, Whistler JL. Dopamine D(3) receptors are down-regulated following heterologous endocytosis by a specific interaction with G protein-coupled receptor-associated sorting protein-1. *J Biol Chem*. 2011;286:1598–608.
82. Chazalon M, Paredes-Rodriguez E, Morin S, Martinez A, Cristovao-Ferreira S, Vaz S, et al. GAT-3 Dysfunction Generates Tonic Inhibition in External Globus Pallidus Neurons in Parkinsonian Rodents. *Cell Rep*. 2018;23:1678–90.
83. Adermark L, Lagström O, Loftén A, Licheri V, Havenäng A, Loi EA, et al. Astrocytes modulate extracellular neurotransmitter levels and excitatory neurotransmission in dorsolateral striatum via dopamine D2 receptor signaling. *Neuropsychopharmacology*. 2022;47:1493–1502. <https://doi.org/10.1038/s41386-021-01232-x>. Epub 2021 Nov 22.
84. Jiang M, Chen G. Ca²⁺ regulation of dynamin-independent endocytosis in cortical astrocytes. *J Neurosci*. 2009;29:8063–74.
85. Boulay AC, Saubamea B, Adam N, Chasseigneaux S, Mazare N, Gilbert A, et al. Translation in astrocyte distal processes sets molecular heterogeneity at the gliovascular interface. *Cell Disco*. 2017;3:17005.
86. Xin H, Wang F, Li Y, Lu QE, Cheung WL, Zhang Y, et al. Secondary Release of Exosomes From Astrocytes Contributes to the Increase in Neural Plasticity and Improvement of Functional Recovery After Stroke in Rats Treated With Exosomes Harvested From MicroRNA 133b-Overexpressing Multipotent Mesenchymal Stromal Cells. *Cell Transpl*. 2017;26:243–57.

ACKNOWLEDGEMENTS

We thank M. Morini, E. Albanesi, D. Cantatore, G. Pruzzo, T. Catelani, D. Mauro, S. Monari, F. Torri, B. Chiarenza, A. Monteforte and C. Chiabrera, for technical support. We thank GlaxoSmithKline and Dr S. Wilson for generously donating the newly generated Dys1A^{flox} mice. We thank Dr D.R. Weinberger and Dr R.E. Straub for initial access to the Brain Cloud databank. This work was supported by funding from the Marie Skłodowska-Curie Fellowships (grant n.796244) to CD; the Ministero

dell'Università e della Ricerca italiano (project PRIN 2017K2NEF4) to FD; grant MIUR Progetto eccellenza to FF; the Istituto Italiano di Tecnologia, the Brain and Behavior Research Foundation (2015 NARSAD grant n.23234), the Ministero della Salute italiano (project GR-2016-02362413), and Fondazione Telethon Italia (project GGP19103) to FP.

AUTHOR CONTRIBUTIONS

Conceptualization, RM, GT, and FP; Methodology and Investigation, RM, GT, DD, CD, GL, AL, LC, FF, VF, GO, RM, FM, GP, AF, GC, MADL, FM, and FP; Resources, GO, DR, JLW, GML, GC, CSW, and FP; Writing, all authors; Visualization, RM, GT, DD, CD, GL, AL, GL, GO, RM, FM, and FP; Supervision, FP; Funding Acquisition, FD, CSW, and FP.

COMPETING INTERESTS

The authors declare no competing interests.

ADDITIONAL INFORMATION

Supplementary information The online version contains supplementary material available at <https://doi.org/10.1038/s41380-022-01683-8>.

Correspondence and requests for materials should be addressed to Francesca Managò or Francesco Papaleo.

Reprints and permission information is available at <http://www.nature.com/reprints>

Publisher's note Springer Nature remains neutral with regard to jurisdictional claims in published maps and institutional affiliations.